“A damage model for the frictional shear failure of brittle materials in compression”

Simon P. A. Gill

This manuscript has been submitted for publication in COMPUTER METHODS IN APPLIED MECHANICS AND ENGINEERING. Please note that the manuscript has not undergone peer review. Subsequent versions of this manuscript may have different content. If accepted, the final version of this manuscript will be available via the “peer---reviewed Publication DOI” link on the right-hand side of this webpage.

Please feel free to contact the author directly to comment on the manuscript. Constructive feedback is welcomed.

A damage model for the frictional shear failure of brittle materials in compression

Simon P.A. Gill

Email: spg3@le.ac.uk

School of Engineering
University of Leicester
University Road
Leicester
LE1 7RH, UK

Abstract

Damage models have been successfully employed for many decades in the modelling of tensile failure, where the crack surfaces separate as a crack grows. The advantage of this approach is that crack trajectories can be computed simply and efficiently on a fixed finite element mesh without explicit tracking. The development of damage models for shear failure in compression, where the crack faces slide over each other subject to friction, is a non-trivial extension of this approach. A major difference is that part of the material stiffness in the damaged region must be retained to avoid interpenetration of the crack faces. This problem is resolved here by employing an anisotropic modification to the elastic stiffness tensor in the damaged region. This has the benefit of driving frictional cracks into the correct orientation, according to the Mohr-Coulomb failure criteria, but three issues remain. The first is that the shear discontinuity introduces some spurious stress perturbations around crack regions that are narrow (less than 3-4 elements wide). This is ameliorated by Helmholtz smoothing to allow efficient simulation on a coarse mesh. The second is that the complementarity of shear stress means that the shear stiffness is removed normal to the crack interface as well as parallel to it, and the third is that there are two potentially active failure planes at each point. Both these latter two issues are resolved by the introduction of a novel failure plane selection variable, which regulates either single plane or dual plane failure, and prevents the growth of erroneous cracks normal to the crack face. Both local and non-local models are investigated for linear and exponential strain softening responses. Unlike the non-local model, the local model demonstrates some mesh-size dependence, but it still retains some properties of interest, in that it supports narrower cracks and more rapidly forms a preference for the growth of a single crack when there are a number of competing cracks. The model is implemented in commercial finite element package COMSOL Multiphysics v5.5 and validated against two benchmark simulations: biaxial compression and the failure of a 45^o slope. The correct crack angles, stipulated by the Mohr-Coulomb friction angle, are correctly reproduced, as is the post-failure residual frictional force in biaxial compression. The effect of the shear fracture energy on the force-displacement response is investigated, demonstrating the successful simulation of the range of material behaviour expected in geological samples, from broad ranged gradual collapse to sharp, almost instantaneous failure.

PREPRINT: A damage model for the frictional shear failure of brittle materials in compression

1. Introduction

The shear failure of brittle materials in compression is of practical interest in structural geology and engineering [1]. Mathematical modelling of the growth of opening cracks in tension has been widely studied [2-27], whereas the growth of non-opening, frictional sliding cracks in compression has received less attention. A range of methods and models have been proposed for modelling brittle and ductile crack opening problems: continuum-based models such as the finite element method (FEM) [2], the extended finite element method (XFEM) [2,4], the phase field method [5-20], damage models [21-25], the numerical manifold method [26] and the material point erosion method [27]. Closed crack problems for modelling brittle materials in compression range from the finite-discrete element method (FDEM) [28] to damage models [29-33], phase field models [34-38] as well as particle-based models [39-42] and plasticity models [37]. The main advantage of phase field and damage models is that no complex interface tracking is necessary to determine the crack path. This means that simulations can be performed on a fixed finite element mesh and can often be implemented in commercial finite element software. Some of these crack-opening techniques have been adapted to the case of compressive failure, but often without complete physical validation. For instance, a number of damage models have adopted the isotropic damage model of the crack opening methods, which typically degrades the entire elastic modulus of the material [29-31] in the damaged zone. The consequence of this simple approach is that crack faces can overlap in the compressive state. As well as being unphysical, this makes correct determination of the normal pressure acting on the crack face impossible, and hence another consequence is the lack of treatment of the friction that exists between the crack surfaces as they slide over each other. Degrading just the shear modulus [33,43,44] is another damage model approach. This can be reasonable in the absence of friction, although not strictly correct as it degrades shear stiffness in every direction, whereas it should just be degraded in the plane of the crack face. Spectral decomposition of the strain energy [18,36,38] is also used in phase field models, where the positive and negative strain contributions are separated, although this is generally applied to crack opening problems where only the tensile contribution drives crack growth [18].

The Mohr-Coulomb condition is adopted here. This is widely used in geology for the frictional shear failure of brittle materials in compression. The coefficient of friction is $\tan\phi$, where the friction angle ϕ is measured from the orientation θ of the dominant shear crack in a failure specimen subject to confined compression [1]. The angle $\theta = 45^o - \frac{\phi}{2}$ is the angle between the crack face tangent and the maximum principal compressive stress. Reproduction of this angle in a representative simulation is therefore an important measure of its efficacy. Recently Fei and Choo [34,45,46] have made important progress in this area in the context of the phase field method, and are the first to clearly demonstrate that they can reproduce the expected frictional crack angle θ in biaxial compression tests. This is achieved through the implementation of an anisotropic elastic degradation model. This approach is adopted here, but in the context of a damage model.

The phase field and damage modelling approaches have similarities, but also essential differences. In a recent comparative study, Mandel et al [47] have compared the phase field and damage models for tensile (opening) mode I and mixed-mode crack growth. Whilst concluding that both methods are suitable for modelling the initiation and propagation of cohesive cracks, the phase field method has the advantage of being insensitive to the length scale of the model, as long as the mesh is sufficiently fine. In the damage model there is a strong relationship between the material properties and the mesh size [48], also demonstrated in this paper, although the macroscopic response can be shown to be independent of mesh size if treated correctly. The main stated advantage of damage models is that

they "…are computationally efficient and thus suitable for large-scale engineering simulations, phase field methods are quite demanding and therefore currently limited to small-scale problems." [47]. As such, it is an objective of this paper to develop an efficient damage model for frictional shear failure that employs the minimum number of degrees-of-freedom. Another objective is to develop the algorithm within the context of a commercial finite element package, in this case COMSOL Multiphysics v5.5, such that it is readily implemented within an existing numerical framework without specialist routines or coding. The model is implemented in two-dimensions in this paper for numerical benchmarking against the biaxial compression and slope stability cases of Fei and Choo [34] in sections 4 and 5. However the method is sufficiently efficient to be practically implemented in three-dimensions. The basic damage model is defined in section 2 and the anisotropic elastic degradation model is tested in section 3, highlighting its advantages and disadvantages. Necessary adaptions to the damage model are subsequently introduced in section 4 in the light of this, where initially some of the pitfalls of compressive shear failure modelling are illustrated in the context of uniaxial compression testing, followed by validation against appropriate benchmark simulations.

2. The damage model

The focus of this paper is the development of a model for the initiation and propagation of one or more dominant shear cracks in compression. In practice geological materials can fail in a number of different ways [1]. Depending on the confining pressure, the water content, pore pressure, and temperature, the response can be either brittle or ductile, or a combination of both. Failure can be due to the accumulation of micro-cracks, often in tension, which may finally amalgamate into a dominant compressive shear crack when the material eventually fails. These various failure modes can be incorporated into a model using various approaches (e.g. [49]) but this work is concerned with the growth of dominant shear cracks. Most brittle materials contain pre-existing flaws/pores, which if they are small can be represented by material heterogeneity [31,32,50], or if they are large, clearly defined joints [28] or faults [31]. Again, there is no reason that these effects cannot be incorporated in to the proposed framework, but here the focus is on brittle shear failure of a homogeneous material with no pre-existing flaws, defined by the Mohr-Coulomb failure condition.

2.1 Damage formulation

The standard isotropic damage model for tensile failure introduces a damage parameter $w \in [0,1]$ which degrades the material stiffness in the damaged zone, such that

$$\sigma_{ij} = (1 - w)C_{ijkl}\epsilon_{kl} \tag{1}$$

where $w = 0$ in the undamaged state and $w = 1$ in the fully damaged state, σ_{ij} is the stress tensor, C_{ijkl} is the elasticity tensor and ϵ_{ij} is the strain tensor, with $i, j = 1,2,3$. This model works well in tension, where the crack faces separate with increasing load, but not in compression, as it allows interpenetration of the crack faces. Hence a more general anisotropic degradation of the modulus is required

$$\sigma_{ij} = \left(C_{ijkl} - wC^{\tau}_{ijkl}\right)\epsilon_{kl} \tag{2}$$

where the elastic stiffness tensor C^{τ}_{ijkl} is such that it degrades the shear stress τ parallel to the crack face whilst preserving the normal stresses acting on the crack face to avoid interpenetration. There is also a frictional force between the crack faces which resists sliding. Physically it seems more appropriate to implement this through the addition of an external friction stress

$$\sigma_{ij} = \left(C_{ijkl} - wC^{\tau}_{ijkl}\right)\epsilon_{kl} + w\sigma^{f}_{ij} \tag{3}$$

The form of these two contributions is derived in section 2.3. The stiffness degradation can also be implemented in the form of an external stress, $\sigma^{\tau}_{ij} = C^{\tau}_{ijkl}\epsilon_{ij}$, but it is found that the proposed elastic stiffness tensor formulation is numerically more stable.

A damage model requires a constitutive law which relates the damage level to strain. Two different strain softening models are investigated here, linear and exponential, as shown in the stress-strain relationships of Figure 1. In the absence of friction, the degraded shear stress post-failure initiation is $\tau = \left(1 - w(\gamma)\right)\mu\gamma = Cg(\gamma)$, where μ is the shear modulus, γ is the total shear strain, $C = \mu\gamma_0$ is the cohesive strength and γ_0 is the shear strain at which failure commences, such that $w(\gamma_0) = 0$. The general form of the damage model is then

$$w(\kappa) = 1 - \frac{\gamma_0}{\kappa}\, g(\kappa) \tag{4}$$

for $\kappa \geq \gamma_0$, and zero otherwise, where κ is a measure of the strain history at a point. For linear strain softening

$$g(\kappa) = \max\left(0, \frac{\gamma_f - \kappa}{\gamma_f - \gamma_0}\right) \tag{5}$$

where the failure strain satisfies $w\left(\gamma_f\right) = 1$ and is related to the critical energy release rate in shear G_{II} by

$$\gamma_f = \frac{2G_{II}}{Ch_{cb}} \tag{6}$$

as, from equation (39), the critical energy release rate G_{II} [51] is the area under the stress strain curve in the absence of the frictional contribution, and $h_{cb}$is the width of the shear crack band.

For exponential strain softening

$$g(\kappa) = \exp\left(-\frac{\kappa - \gamma_0}{\gamma_c - \gamma_0}\right) \tag{7}$$

where in this case there is no absolute failure strain ($\gamma_f \to \infty$) but the critical strain is given by

$$\gamma_c = \frac{G_{II}}{Ch_{cb}} + \frac{\gamma_0}{2}$$

(8)

using equation (39).

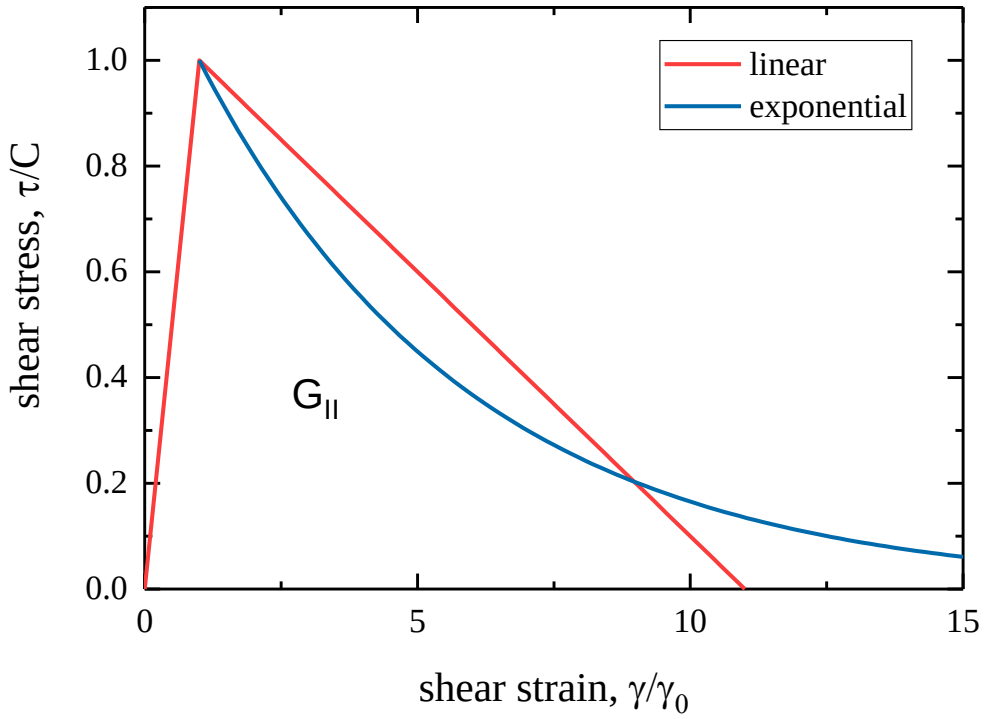

Figure 1 : Shear stress- shear strain relationships for the linear and exponential damage models in the absence of friction, i.e. when the stress normal to the crack face is zero such that $p_n = 0$.

For failure in the presence of friction, κ is defined by an appropriate strain measure, γ_{eq}, defined in section 2.2. Two approaches are considered here. The *local model* uses the raw discontinuous equivalent strain stored at the Gauss points

$$\kappa = \gamma_{eq}$$

(9)

The *non-local model* uses a smoothed continuous equivalent strain defined at the nodes

$$\kappa = \tilde{\gamma}_{eq}$$

(10)

where the Helmholtz equation is used to smooth the local strain measure

$$\tilde{\gamma}_{eq} - c_\gamma \nabla^2 \tilde{\gamma}_{eq} = \gamma_{eq}$$

(11)

where the parameter $c_\gamma = \frac{1}{2} l_\gamma^2$, where l_γ defines the smoothing length for the shear strain field. Note that when $c_\gamma = 0$ equation (11) still has an effect as it projects the discontinuous strain field defined

at the Gauss points onto a continuous strain field defined at the nodes. However, to avoid the appearance of spurious artefacts in the smoothed strain field, it is advised that the smoothing length is greater or equal to the distance between Gauss points [30].

As damage is irreversible, it is common to use the maximum value of the equivalent strain history at a point

$$\kappa_{\max} = \max(\kappa(\eta),0) \quad \eta \in [0,t] \tag{12}$$

to satisfy the Kuhn-Tucker condition, i.e. damage can never decrease such that $\dot{w}(\kappa_{\max}) \geq 0$. However, failure in brittle materials is often characterised by rapid crack growth, i.e. fast fracture. Inertial effects are ignored here, and as such the crack growth rate is effectively unconstrained. This numerically unstable situation can be avoided by using viscous regularisation rather than equation (12). In this case the maximum value of the strain measure is evolved according to

$$\frac{d\kappa_{\max}}{dt} = k(\kappa - \kappa_{\max})(\kappa > \kappa_{\max}) \tag{13}$$

where here a logical condition such as $(\kappa > \kappa_{\max})$ is 1 if true and 0 if false. The strain measure $\kappa_{\max}$ is stored as fourth order Gauss point data, such that there are 10 Gauss points for triangular elements and 16 Gauss points for quadrahedral elements. This higher order Gaussian quadrature is preferential for the non-local model (enhanced stability) but essential for the successful implementation of the local model, due to the variation in the elastic modulus within a damaged element. Equation (13) also has the advantage that it is trivial to implement, whereas the Kuhn-Tucker condition requires specialist code.

2.2 Mohr-Coulomb failure model

The Mohr-Coulomb material failure model defines the equivalent strain measure γ_{eq} for the damage model. The failure criteria is written in terms of stress as

$$|\tau| = p_n tan\phi + C \tag{14}$$

where τ is the shear stress on the failure plane (crack face), p_n is the compressive stress acting normal to the failure plane, ϕ is the friction angle and C is the cohesive strength before failure. After failure the frictional component of the shear stress on the failure plane remains such that $|\tau| = p_n tan\phi_r$, where ϕ_r is the residual friction angle after failure. Note that the frictional term in equation (14) is only non-zero if the normal stress is compressive. Here compressive stresses are taken to be positive, such that friction is active when $p_n > 0$. In the absence of friction ($\phi = 0$ or $p_n = 0$) this reduces to the simple failure condition $|\tau| = C$ considered in section 2.1. The scenario whereby tensile failure is active ($p_n < 0$) is not considered in this paper but is easily incorporated into the model using the standard approach for opening cracks [21-25].

The shear stress τ and normal stress p_n depend on the angle of orientation of the stress state θ to the principal stress directions. Here the maximum and minimum (compressive) principal stresses in 2D are

σ_1 and σ_2 respectively, where $\sigma_1 \geq \sigma_2$. Mohr's circle provides the relationship between these quantities, as shown in Figure 2. Here a positive shear stress couple is taken to act anti-clockwise.

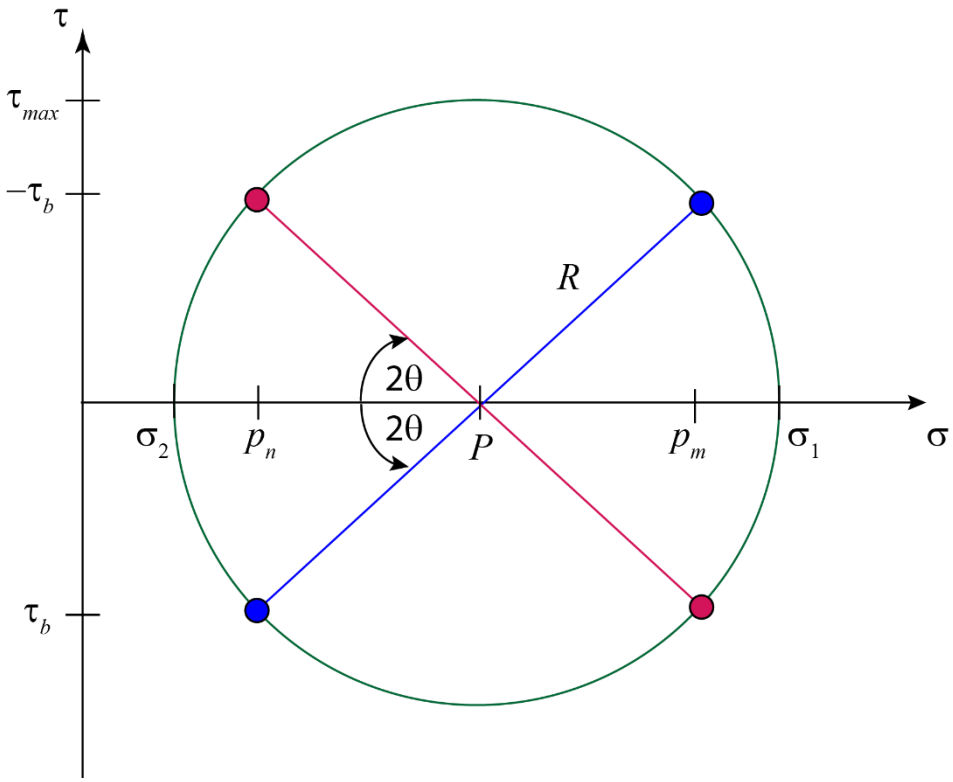

Figure 2: Mohr's circle illustrates the relationship between the shear stress τ and the normal stress p_n on two equivalent failure planes, blue $(+)$ and red $(-)$, at an angle $\pm\theta$ to the direction of minimum compressive stress σ_2 respectively.

There are two identical stress state solutions, indicated by the blue and red lines in Figure 2. These two states are furthermore denoted by the superscripts $(+)$ and $(-)$ respectively. For a shear plane orientated at an angle θ from the direction of minimum principal compressive stress σ_2, the shear stress is $|\tau| = \tau_b = Rsin2\theta$ and the normal stress is $p_n = P - Rcos2\theta$, where the hydrostatic pressure $P = \frac{1}{2}(\sigma_1 + \sigma_2)$ is the centre of the circle and the maximum shear stress $R = \tau_{\max} = \frac{1}{2}(\sigma_1 - \sigma_2)$ is the radius of the circle. Note that the normal stress parallel to the slip direction is $p_m = P + Rcos2\theta$. Failure is expected parallel to the slip direction as it is subject to less friction, i.e. $p_n < p_m$. Inserting these stresses into the failure condition (14)

$$\tau_{\max} sin(2\theta + \phi) sec\phi = Ptan\phi + C \tag{15}$$

The orientation of the failure plane is the one that achieves failure first, i.e. when $2\theta + \phi = 90^o$, such that the critical angle is $\theta = 45^o - \frac{\phi}{2}$. The failure condition therefore becomes

$$\tau_{\max} sec\phi = Ptan\phi + C \tag{16}$$

As the stresses are degraded by damage through the reduced stiffness tensor, the failure condition must be written in terms of the strains. For isotropic elasticity under plane strain conditions

$$\tau_{\max} = \mu(\epsilon_1 - \epsilon_2) \qquad and \qquad P = (\lambda + \mu)(\epsilon_1 + \epsilon_2) \tag{17}$$

where ϵ_1 and ϵ_2 are the maximum and minimum principal compressive strains and $\mu = \frac{E}{2(1+\nu)}$ and $\lambda = \frac{\nu E}{(1+\nu)(1-2\nu)}$ are Lamé's constants, and E and ν are the Young's modulus and Poisson's ratio respectively. The failure condition is therefore expressed as

$$\gamma_{eq} = \gamma_0 \tag{18}$$

where $\gamma_0 = \frac{C}{\mu}$ is in the failure initiation strain, as introduced in section 2.1, and the equivalent strain for the Mohr-Coulomb condition is

$$\gamma_{eq} = [(1 - a)\epsilon_1 - (1 + a)\epsilon_2]sec\phi \tag{19}$$

where $a = \frac{sin\phi}{(1-2\nu)}$. In the absence of friction this simply becomes the maximum shear strain, i.e. $\gamma_{eq} = \epsilon_1 - \epsilon_2 = \gamma_{\max}$.

2.3 Stiffness degradation due to damage on a failure plane

There are many methods for accommodating discontinuities, such as crack faces or shear bands, within a finite element (FE) model (see chapter 7 in [52] for a review). However, these typically rely on adapted shape functions within elements to represent the discontinuity, which makes them either difficult or impossible to implement in a commercial FE code, and dilutes the principal benefit of phase field and damage models, which uses a fixed FE mesh without adaptation. Therefore, it is assumed here that any discontinuities can be reasonably well represented by standard elemental shape functions.

Following Fei and Choo [34], the orientation of a failure plane is defined by its slip direction $\underline{m}$ and its normal $\underline{n}$, where the vector pairs are of unit length ($n_i n_i = m_i m_i = 1$) and orthogonal ($n_i m_i = 0$). Given the stress state σ_{ij} at a point, the normal stress p_n is defined by

$$p_n = n_i \sigma_{ij} n_j \tag{20}$$

and the shear stress on the failure plane is given by

$$\tau_b = m_i \sigma_{ij} n_j. \tag{21}$$

The shear stress on each plane can also be written as

$$\tau_b = \frac{1}{2}\alpha_{ij}\sigma_{ij} \tag{22}$$

where, as the stress state is symmetric ($\sigma_{ij} = \sigma_{ji}$), we have introduced

$$\alpha_{ij} = n_i m_j + m_i n_j \tag{23}$$

This tensor is symmetric ($\alpha_{ij} = \alpha_{ji}$) with orthogonality implying $\alpha_{ii} = 0$. In the undamaged state, the stress is related to the strain, $\sigma_{ij} = C_{ijkl}\epsilon_{kl}$, by the standard isotropic elastic stiffness tensor

$$C_{ijkl} = \lambda\delta_{ij}\delta_{kl} + \mu\left(\delta_{ik}\delta_{jl} + \delta_{il}\delta_{jk}\right) \tag{24}$$

Substituting into equation (22)

$$\tau_b = \frac{1}{2}\alpha_{ij}C_{ijkl}\epsilon_{kl} = \frac{1}{2}\alpha_{ij}\left[\lambda\delta_{ij}\delta_{kl} + \mu\left(\delta_{ik}\delta_{jl} + \delta_{il}\delta_{jk}\right)\right]\epsilon_{kl} = \frac{1}{2}[\lambda\alpha_{ii}\delta_{kl} + \mu(\alpha_{kl} + \alpha_{lk})]\epsilon_{kl} \tag{25}$$

yields

$$\tau_b = \mu\alpha_{kl}\epsilon_{kl} \tag{26}$$

Similarly, we have

$$p_n = n_i\sigma_{ij}n_j = [\lambda n_i n_i\delta_{kl} + \mu(n_k n_l + n_l n_k)]\epsilon_{kl} \tag{27}$$

giving

$$p_n = [\lambda\delta_{kl} + 2\mu n_k n_l]\epsilon_{kl} \tag{28}$$

The contribution to the stress tensor from the shear component is

$$\sigma_{ij}^{\tau} = \tau_b\alpha_{ij} = \mu\alpha_{ij}\alpha_{kl}\epsilon_{kl} = C_{ijkl}^{\tau}\epsilon_{kl} \tag{29}$$

where $C_{ijkl}^{\tau} = \mu\alpha_{ij}\alpha_{kl}$, as given by Fei and Choo [34]. No shear stress is supported parallel to a crack face in the absence of friction, and hence this stress contribution must be removed from a damaged region, as shown in equation (2). When friction is active, the frictional shear stress on the interface must be added, as shown in equation (3). This acts in the same plane, defined by the tensor α_{ij}, such that

$$\sigma_{ij}^{f} = -p_n tan\phi sign(\tau_b)\alpha_{ij} \tag{30}$$

if $p_n > 0$ and zero otherwise. Here ϕ_r replaces ϕ once failure is initiated ($w > 0$). In this paper it is assumed that slip (non-stick) conditions always apply. Treatment of the alternative conditions for sticking ($|\tau| < p_n tan\phi_r$) and crack opening ($p_n < 0$) can be found in the phase field context in Fei and Choo [34,45], with more advanced criteria proposed by Bryant and Sun [53].

2.4 *Dual failure plane formulation*

As shown in Figure 2, there are two identical failure planes, with their tangents orientated at a clockwise angle of $\pm\theta$ from the direction of maximum principal compressive strain. Let $\underline{e_1}$ and $\underline{e_2}$ be the principal strain directions for the maximum and minimum compressive strains respectively. Then the slip directions of the two planes, denoted by the superscripts $(+)$ and $(-)$, are

$$\underline{m}^{(\pm)} = cos\theta \underline{e_1} \pm sin\theta \underline{e_2} \tag{31}$$

and the normals are

$$\underline{n}^{(\pm)} = \mp sin\theta \underline{e_1} + cos\theta \underline{e_2} \tag{32}$$

These orientations are indicated in the schematic diagram of Figure 5 for the case of biaxial compression. In this model, the principal strain directions are updated at a point until damage has initiated, as which point they are fixed. Without presuming which failure plane is active, the elastic stiffness tensor of equation (29), to remove shear from the $(+)$ or $(-)$ interface, is

$$C^{\tau}_{ijkl} = \mu(\chi \alpha^{(+)}_{ij}\alpha^{(+)}_{kl} + (1-\chi)\alpha^{(-)}_{ij}\alpha^{(-)}_{ij}) \tag{33}$$

where $\alpha^{(\pm)}_{ij} = n^{(\pm)}_i m^{(\pm)}_j + m^{(\pm)}_i n^{(\pm)}_j$ from equation (23). The variable $0 \leq \chi \leq 1$ selects the active failure plane. If $\chi = 1$ then the $(+)$ plane is active and if $\chi = 0$ then the $(-)$ plane is active. It is expected that only one failure plane is active at a given point in space and time, i.e. χ is zero or one. Equation (33) is equivalent to equation (29) if $\chi = 1$.

Similarly

$$\sigma^f_{ij} = -p_n tan\phi \left[\chi sign\left(\tau^{(+)}_b\right)\alpha^{(+)}_{ij} + (1-\chi) sign\left(\tau^{(-)}_b\right)\alpha^{(-)}_{ij}\right] \tag{34}$$

where, from equation (21), we have $\tau^{(\pm)}_b = \frac{1}{2}\alpha^{(\pm)}_{ij}\sigma_{ij}$.

3. Test of the elastic degradation model

Here the effectiveness of the elastic degradation model of section 2.3 in removing shear stress from a fully damaged interface is investigated. Equations (2) and (29) are implemented in COMSOL Multiphysics v5.5. Frictional stresses are not added at this stage. Following Fei and Choo [34], a rectangular body, 80 mm x 170 mm, is analysed subject to a vertical compressive displacement δ, as

shown in Figure 3a. The damage parameter, w, is zero everywhere except within a zone of width W at an angle θ to the vertical centered about the middle of the rectangle, where $w = 1$. The modulus and Poisson ration are taken to be E=27 MPa and ν=0.3 and the applied displacement is δ =10mm. The damaged zone is defined independently of the underlying mesh, and is shown in Figure 3a for a triangular mesh with a triangle side of length h=1mm. Fourth order Gaussian integration is used, which equates to 10 and 16 Gauss points per element for triangular and quadrilateral elements respectively. Therefore it is possible that $w = 1$ at some Gauss points within an element, and $w = 0$ at the others. The von Mises stress at the Gauss points is shown under load in Figures 3b to 3d for damage bands of width W=3, 5 and 20mm respectively. In Figure 3b the damage band is 3 elements wide but the residual stress extends significantly beyond that. It is clear that there is a significant, unwanted residual stress state generated by narrow bands (less than 4-5 elements wide). This reduces as the band widens, and is also ameliorated by the more diffuse nature of an actual damage zone. This is particularly the case for very wide damage bands, such as that shown in Figure 3d, where the stress perturbation is only associated with the sharp interface of the damage zone considered here. This case is more typical of the finely resolved interface used for the phase field method of Fei and Choo [34], although it is computationally very expensive. The aim here is to use the minimum number of degrees of freedom as possible to resolve the damage zone, so the consequences of narrower damage zones is explored further.

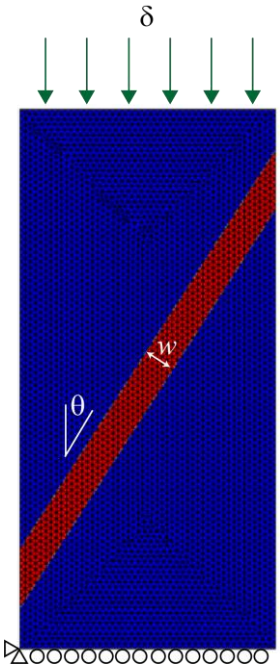

(a)

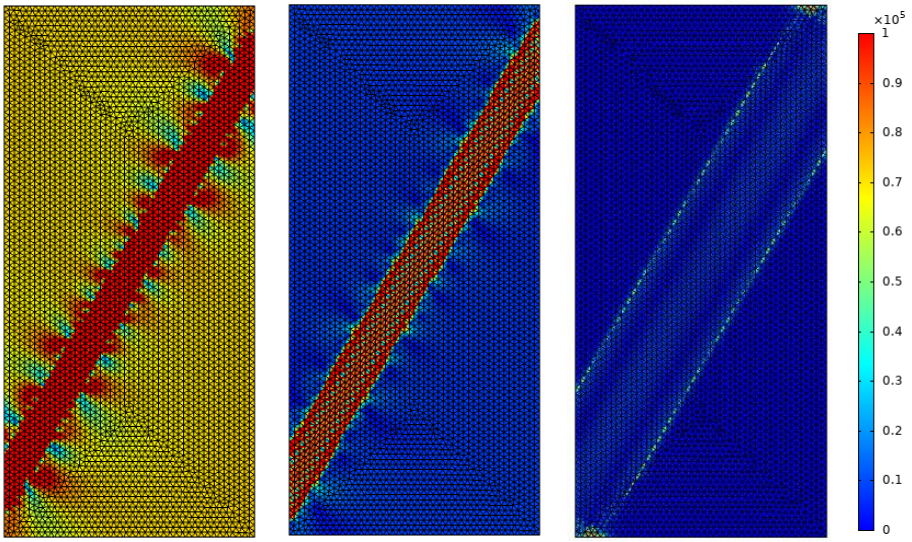

(b) (c) (d)

Figure 3: (a) the damage parameter is set to one in a (red) band of width W at an angle of $\theta = 45 - \frac{\phi}{2}$ to the vertical. Here W=5 mm and $\phi = 30^o$. The von Mises stress is shown for triangular elements with a quadratic shape function for a damage band width of W equal to (b) 3 mm, (c) 5 mm and (d) 20 mm. Each triangular element has a side length of 1mm.

It is expected that zero force should be required to compress the body when it is fully damaged in this way, when friction and gravity are not present. However, the presence of a large stress perturbation adjacent to the damage band results in the occurrence of a residual force. The fraction of the applied force that remains after degradation of the damage band is plotted in Figure 4a for six different situations: “linear” uses linear FE shape functions, “quad” uses quadratic FE shape functions and “quad shear” uses quadratic FE shape functions but, rather than using the anisotropic model of equation (2), the shear modulus μ is simply turned off (reduced to 10^{-6} of its original value) in the damage zone. Each of these three cases is also implemented using the Pressure Formulation (denoted by PF) which is typically used for nearly incompressible materials (where the shear modulus is very small) [42]. In Figure 4a, the linear elements are seen to perform very poorly, and hence should not be used for the elastic analysis. This is in contrast to Crack Band damage models in tension that recommend the use of linear elements. The performance of the quadratic elements is much improved, with the residual force at about 1% for a 5 element wide damage zone. The “quad shear” model performs extremely well for damage zones over 2 elements in width. The Pressure Formulation reduces the residual force in all cases, although its most noticeable effect is on the “quad shear” model with interface widths of 1 and 2 elements. This is not surprising as only the “quad shear” model creates a nearly incompressible material in the damage zone. The results for other friction angles ϕ are similar. Triangular elements perform slightly better than quadrahedral elements, but the difference is not sufficient to strongly recommend one type over the other.

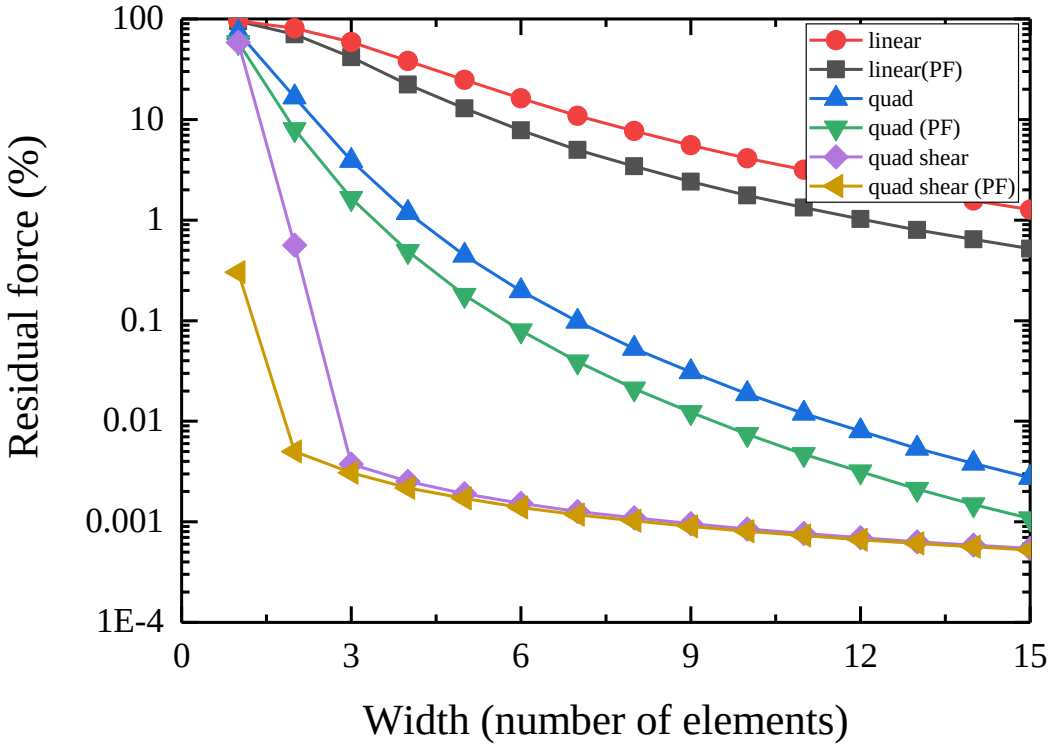
Residual force (%)
100
10
1
0.1
0.01
0.001
1E-4
0
3
6
9
12
15
Width (number of elements)
linear
linear(PF)
quad
quad (PF)
quad shear
quad shear (PF)

(a)

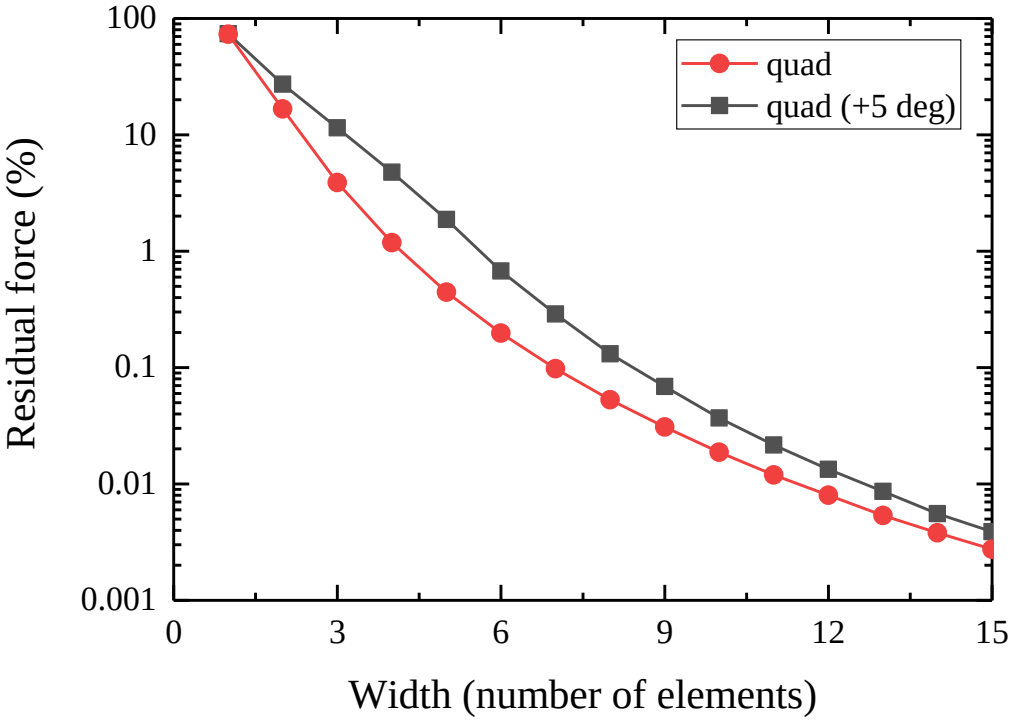
Residual force (%)
100
10
1
0.1
0.01
0.001
0
3
6
9
12
15
Width (number of elements)
quad
quad (+5 deg)

(b)

Figure 4: (a) The percentage residual force that remains as a function of the width of the damage band W (in terms of number of triangular elements) for $\phi = 15^o$. (b) Effect of the misalignment between the damage stress and the damage band on the residual force. The black line shows the residual force when the misalignment angle is 5 degrees. The red line shows the fully aligned result.

Unfortunately the simple isotropic "quad shear" approach of degrading the shear modulus in the damage zone does not produce the expected orientation of the failure plane $\theta = 45^o - \frac{\phi}{2}$ in the full damage model (described in section 4). In this case the shear crack is always orientated at 45^o, regardless of the failure criteria. Hence this is not an viable approach. It does show, however, that the anisotropic elasticity model of equation (2) is key to generating cracks in the correct orientation. With this is mind, the strength of this orientational effect is investigated in Figure 4b for the "quad" model. This shows how the percentage residual force changes if there is a misorientation between the applied shear stress and the damage zone. Here the orientation of the shear stress (α_{ij}) is calculated for $\phi = 30^o$ and the damage zone is orientated at $\phi = 35^o$. The residual force in the misaligned case is higher than in the aligned case, as one would expect. The absolute difference between the two cases reduces as the interface becomes wider, suggesting that that energetic penalty for misorientation also reduces.

In conclusion, the "quad" model is best adopted. It can be seen from Figure 4a that the residual force is only acceptable (<1%) in this case for a damage band that is 4 elements or more wide. It can be seen from Figure 4b that there is still a strong orientational effect at this width. Hence a crack band of 4-5 elements in width appears to be a desirable compromise between maximising numerical efficiency, minimising unphysical friction and still achieving a strongly directed crack band. The width of the damage band can be adjusted by fine tuning of the non-local strain model, but is not an adjustable parameter in the local strain model. In practice it is found in section 4 that a crack propagates as a narrow damage band that is 1-2 elements wide, but which then naturally broadens over time to 4-5 elements in width in order to reduce the unphysical friction in the interface. In general the elasticity model of equation (2) is found to be adequate for modelling compressive frictional shear damage, but the stress perturbations around the interface, as seen particularly in Figure 3b, mean that additional smoothing of certain quantities is required to remove their deleterious effects. This is clarified in the next section.

4. Uniaxial and biaxial compression tests

Motivated by the test cases of Fei and Choo [34], the failure of a rectangular block under compression is considered for direct comparison, as shown in Figure 5. The rectangle is the same size, 80mm x 170mm, and the material parameters are the same, with $\mu = 10\ MPa$, $\nu = 0.3$, $C = 40\ kPa$, $\phi = \phi_r = 15^o$ and $G_{II} = 30\ J/m^2$. These are typical for an overconsolidated clay, which is a relatively weak material. This yields an initiation strain of $\gamma_0 = 0.4\%$ with a large failure strain of $\gamma_f = 50\%$ for the linear softening model of equation (5) and a large critical strain of $\gamma_c = 25.2\%$ for the exponential softening model of equation (7). The upper surface is subjected to a uniform downward displacement δ which increases over time, and the vertical sides experience a constant inward confining pressure p_c. The material is assumed to be isotropic, homogeneous and with no pre-existing flaws. All models are implemented in COMSOL Multiphysics v5.5 using standard physics options: structural mechanics using quadratic Lagrangian shape functions for the elasticity problem of equation (3), domain ODEs

(ordinary differential equations) using order 4 Gauss point data for the viscous regularisation of equation (13) and the Helmholtz equation using linear Lagrangian shape functions for the smoothing operations of equations (11), (35) and (37). A fully coupled solver is used as this accommodates a larger time step.

There are a couple of minor differences between the model setup employed here and that of Fei and Choo [34]. Firstly, they initiate damage from a weak spot but here a 2mm radius circular hole is introduced into the centre of the sample in order to initiate crack growth. This is because the selected material parameters are for a very gradually softening material, i.e. the fracture energy is high relative to the low cohesive strength, with $\gamma_f = 125\gamma_0$. In this case the damage model requires a well-defined initiation point, otherwise extensive global damage can occur before a dominant crack arises. This is not considered a deficiency of the damage model, but it tends to function better with more rapidly softening materials, i.e. the more brittle materials which this model aims to simulate. In general, it is observed that the proposed damage model and the comparable phase field model [34] behave somewhat differently, with these parameters at least. In the phase field approach, it can be seen that a crack propagates completely through the sample at a relatively low damage level ($w \approx 0.5$) with the damage subsequently increasing to unity to achieve full cleavage. In this damage model the crack propagates in a near to fully damaged state. This is more consistent with the growth of a single dominant crack, as opposed to the amalgamation of many microcracks. This damage model result means that a growing crack has a stronger effect on the stress state ahead of it as it extends, particularly as it approaches another geometric feature, such as a free surface.

The second difference is that Fei and Choo [34] consider biaxial compression, i.e. cases with a non-zero confining pressure p_c. This may be because, without a confining pressure, many brittle materials fail by longitudinal splitting [18], rather than shear fracture [1]. However, here the case of uniaxial compression ($p_c = 0$) is considered before biaxial compression. This proves to be slightly more demanding, as the friction on the fractured interface is expected to be zero, and hence it is considered a more stringent test of the algorithm, whether it is physically realistic or not.

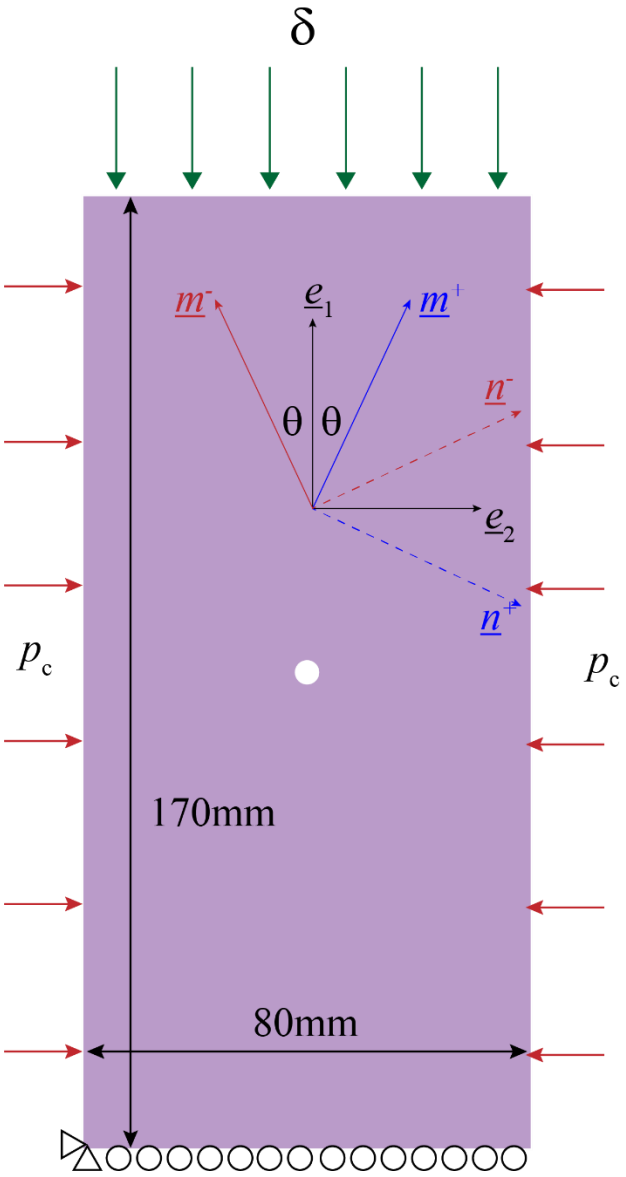

Figure 5: Schematic of the compression test geometry. The rectangle is subject to an increasing downward displacement δ over time. The side walls can be subject to a confining pressure p_c. A small hole of radius 2mm is placed at the centre of the sample to initiate damage growth. Away from the hole, the maximum and minimum principal strain directions $\underline{e}_1$ and $\underline{e}_2$ are as indicated. The orientation of the failure planes, $\underline{m}^{(\pm)}$, and their normals, $\underline{n}^{(\pm)}$, are at an angle of $\pm\theta$ to the maximum principal strain direction, where the $(+)$ failure plane is shown in blue and the $(-)$ system in red, and $\theta = 45^o - \frac{\phi}{2}$.

For the crack band width in equations (6) and (8), from observation we take $h_{cb} = 3h$ for the local model and $h_{cb} = 3h_{\max}$ for the non-local model, where h is the side length of an individual element (triangular or quadrilateral) and $h_{\max} = \max(h)$ is the maximum specified side length in the mesh. The displacement is applied at 1 mm/s and the rate constant for maximum strain evolution is $k = 1000\ s^{-1}$. Increasing the value of k does not change the result. The maximum time step is 0.01s, and can be lower during crack propagation. For the non-local model a very small smoothing length of $l_\gamma =$

$\frac{h_{\max}}{4}$ is required for the failure plane selector χ of equations (33) and (34) to function. This is explained in detail the section 4.1. Due to the stress perturbation around a damaged zone, as shown in Figure 3b, it is necessary to utilise a smoothed version of the normal stress on the boundary $\tilde{p}_n$ in the same manner as equation (11)

$$\tilde{p}_n - c_p \nabla^2 \tilde{p}_n = p_n \tag{35}$$

where the parameter $c_p = \frac{1}{2} l_p^2$, where l_p defines the smoothing length for the normal pressure. As the perturbation is induced on the length scale of the mesh itself, the smoothing length is taken to be $l_p = 5h_{\max}$.

Key parameters

A key parameter in the performance of the damage model is the ratio of the failure (or critical) strain to the damage initiation strain, i.e. the ratio of the width of the undamaged (elastic) and damaged (softening) regions of the stress-strain curves in Figure 1. For the linear strain softening model we adopt the parameter $\beta_{lin} = \frac{\gamma_f}{\gamma_0} - 1 = \frac{2G_{II}\mu}{C^2 h_{cb}} - 1$. For the exponential strain softening model we have $\beta_{\exp} = \frac{\gamma_c}{\gamma_0} - 1 = \frac{1}{2}\left(\frac{2G_{II}\mu}{C^2 h_{cb}} - 1\right) = \frac{1}{2}\beta_{\text{lin}}$. Thus for the material parameters adopted here we have $\beta_{\exp}$ =62 and $\beta_{\text{lin}} = 124$. In this paper the exponential strain softening model is adopted in all cases due to its faster initial softening rate, except for comparison with the linear softening model in Figure 13b. It is required that $\beta_{\exp} > 0$. In practice the damage model achieves the best convergence for values of $1 \leq \beta_{\exp} \leq 100$ with a viscous regularisation of $k = 1000\ s^{-1}$. For $\beta_{\exp} > 100$ the material is too soft such that the damage process is smeared out to the extent that widespread global damage occurs rather than localised damage. For $\beta_{\exp} < 1$ the system is quite stiff, leading to rapid failure which can be numerically harder to solve. In practice many brittle materials have $\beta_{\exp} < 1$. These cases can be modelled by decreasing k (so that the damage evolves more slowly) or by accepting that damage already occurs extremely rapidly for $\beta_{\exp} = 1$ and that increasing the crack propagation rate is unlikely to make much substantial difference to the behaviour.

For rocks one typically finds a friction coefficient of $\tan\phi = 0.1 - 1$, equivalent to fraction angles in the range of $5^o - 45^o$ [1]. Other representative order-of-magnitude material properties for a dry rock at room temperature and pressure are a cohesive strength of $C = 10MPa$ and a shear modulus of $\mu = 10GPa$ and a shear fracture energy of $G_{II} = 10\ J/m^2$. This gives values of $\gamma_0 = 0.1\%$ and $\gamma_c = \frac{10^{-4} G_{II}}{h_{cb}} + \frac{\gamma_0}{2}$. Given $\gamma_c > \gamma_0$ this requires $h_{cb} < 2mm$. The stronger condition of $\beta_{\exp} > 1$ requires that $h_{cb} < \frac{2}{3}mm$. This mesh size is feasible when considering the current sub-metre sized sample, but quickly becomes less feasible for larger samples, which may extend to the kilometre scale. Note that larger values of shear fracture energy have been reported, with values of order-of-magnitude of $G_{II} = 10^4\ J/m^2$ for granite [54], and $G_{II} = 10 - 10^4\ J/m^2$ for stiff clays and shales, depending of the normal stress on the crack face [55].

4.1 Single active failure plane tests

In these first examples, only the $(+)$ failure plane is activated (i.e $\chi = 1$) to illustrate some of the issues to be avoided when modelling compressive shear cracks with friction. The initial calculations are for the exponential strain softening model of equation (7) and an unstructured triangular mesh with $h_{\max} = 1mm$. The mesh is more finely resolved around the circular hole, with side lengths of 0.5mm.

Removing erroneous fracture normal to the failure plane

The first issue to resolve is that the degraded anisotropic modulus C^{τ}_{ijkl} of equation (2) acts equally strongly normal to the failure plane as well as parallel to it, i.e. the shear stress is complementary such that the material stiffness is degraded parallel to $\underline{n}^{(+)}$ as well as parallel to $\underline{m}^{(+)}$. The frictional force is higher parallel to $\underline{n}^{(+)}$ (as $p_m > p_n$) so this does not occur in practice. However, the direction of damage propagation is not known at a point, so there is an equal driving force for crack growth parallel to $\underline{n}^{(+)}$ as there is parallel to $\underline{m}^{(+)}$. This is illustrated in Figures 6 and 7 for the local model and the non-local model respectively. All damage plots are unsmoothed for maximum clarity, such that the raw Gauss point values are plotted, i.e. the values are not interpolated between the nodes. In the early stages it can be seen that in both cases four cracks emanate from the hole, two parallel to $\underline{n}^{(+)}$ and two parallel to $\underline{m}^{(+)}$. For the local model, the steeper cracks, parallel to $\underline{m}^{(+)}$, become dominant and cleave the sample as expected. The crack widens with the mesh size as it gets further from the hole. The final crack width is 2-3 elements wide (2-3 mm) although, as shown in Figure 6c, the shear strain forms along an intense band only 1 element in thickness. The issue with unwanted damage growth normal to the failure plane is even more clearly illustrated by the non-local model in Figure 7b, where the dominant crack erroneously forms at the shallower angle, parallel to $\underline{n}^{(+)}$. Figure 7c shows that the shear displacement of the upper section is to the right rather than to the left in this case. In general the local model favours the creation of a dominant crack earlier than found in the non-local model. This is because smoothing always reduces the maximum strain.

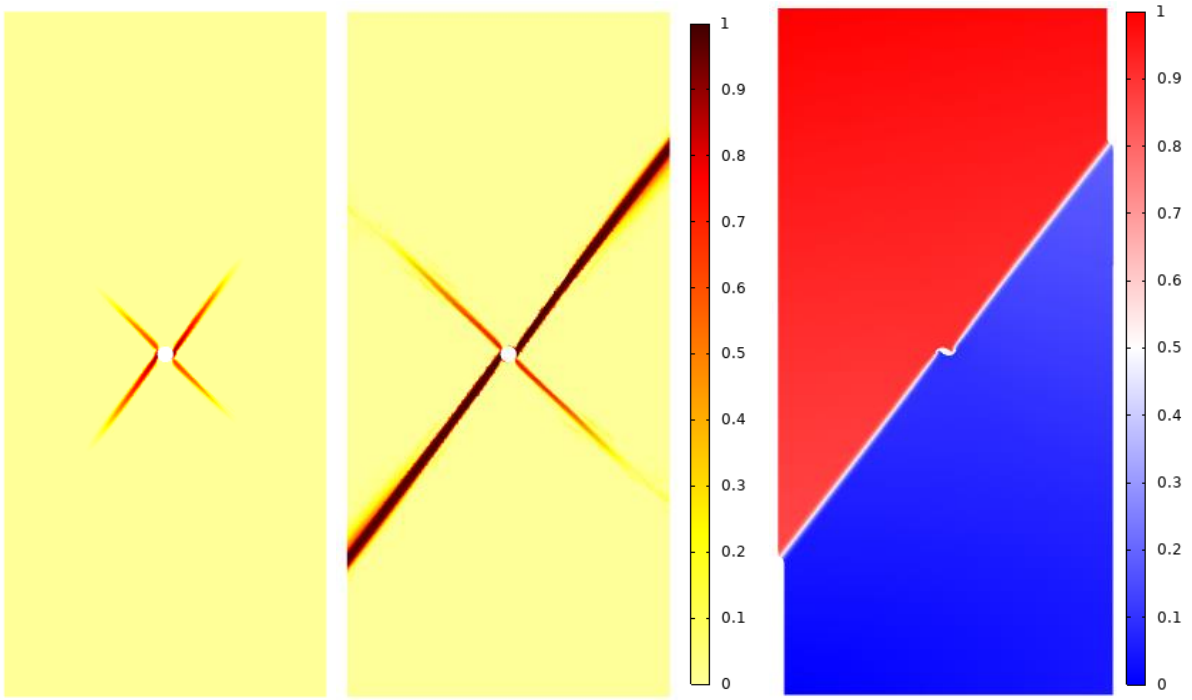

(a) (b) (c)

Figure 6: Uniaxial compression test using the local model with a single active failure plane ($\chi = 1$) for exponential softening: damage w showing erroneous crack growth parallel to $\underline{n}^{(+)}$ (a) the early stages of crack growth when $\delta = 0.57mm$, (b) final cleavage state when $\delta = 0.63mm$. (c) normalised total displacement u_{TOT}/δ and deformed shape of the final state.

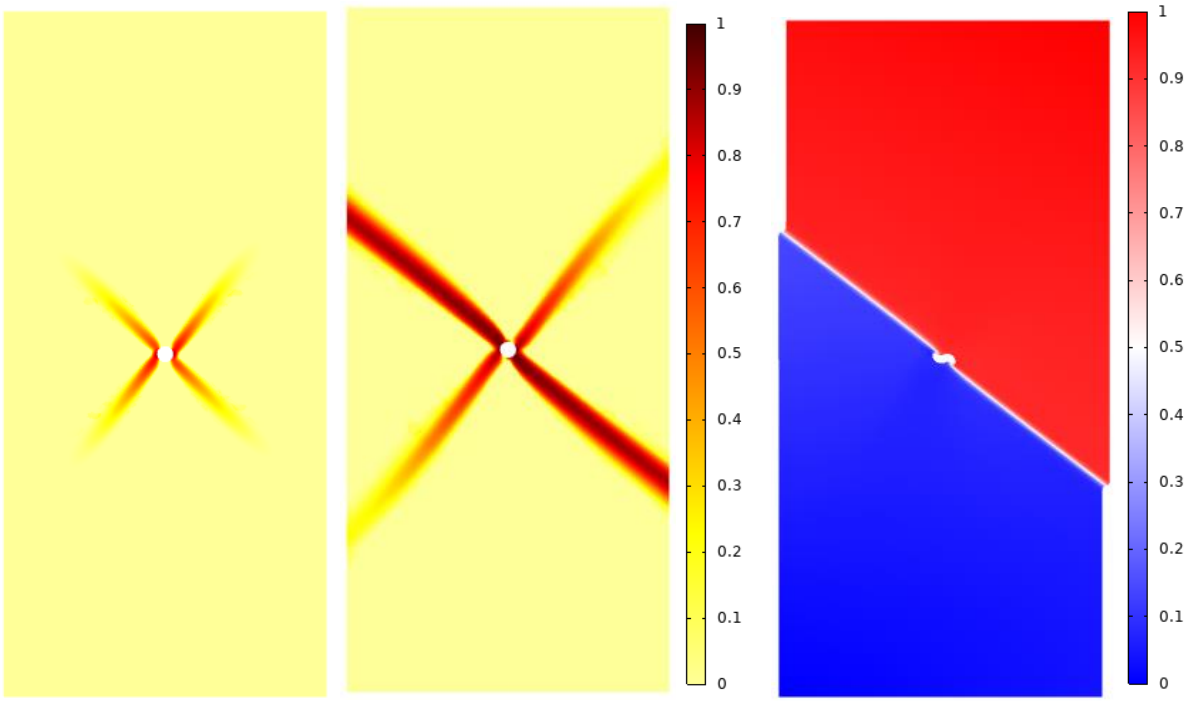

(a) (b) (c)

Figure 7: Uniaxial compression test using the non-local model with a single active failure plane ($\chi = 1$) for exponential softening: damage w showing showing erroneous crack growth parallel to $\underline{n}^{(+)}$ (a) the early stages of crack growth when $\delta = 0.59mm$, (b) final cleavage state when $\delta = 0.64mm$. (c) normalised total displacement u_{TOT}/δ and deformed shape of the final state.

To suppress the erroneous growth of damage normal to the failure plane, it is necessary to determine the growth direction of the damage at every point. Measures can be constructed for this purpose based on the spatial gradient of the damage field. This type of measure is reasonable once the crack has developed, but it is necessary to identify erroneous growth before this point. The shear stress τ_b is found to be a rough but not entirely reliable indicator of the damage growth direction. In practice it is found that the angular rotation ψ at a point is generally an excellent measure of the direction of crack growth, even before damage develops. The rotation of interest is in the plane defined as

$$\psi = \underline{e}_3 . curl \underline{u} = \frac{\partial v}{\partial x} - \frac{\partial u}{\partial y} \tag{36}$$

where $\underline{u} = [u, v, w]$ is the displacement vector and $\underline{e}_3 = [0,0,1]$ is the out-of-plane principal stress direction. In three-dimensions it would be the intermediate principal stress direction. Here the rotation is anti-clockwise if $\psi > 0$ and clockwise if $\psi < 0$. For a body subject to an applied displacement $\underline{\delta}$ the expected rotation on the $(\pm)$ failure plane has the same sign as $\underline{e}_3 . (\underline{\delta} \times \underline{m}^{(\pm)})$. In this case we have $\underline{\delta} = [0, -\delta, 0]$ with $\underline{m}^{(+)} = [sin\theta, cos\theta, 0]$ and $\underline{m}^{(-)} = [-sin\theta, cos\theta, 0]$ such that $\underline{e}_3 . \left(\underline{\delta} \times \underline{m}^{(+)}\right) = \delta sin\theta > 0$ and $\underline{e}_3 . \left(\underline{\delta} \times \underline{m}^{(-)}\right) = -\delta sin\theta < 0$. This suggests that the failure plane selector in this example can therefore simply be taken as the sign of the rotation, i.e. $\chi = (\psi > 0)$. However, there are two additional considerations. The first is that, as shown in Figure 3b, the displacement gradients are distorted around the failure plane for a narrow crack. The values are found to vary very strongly across an element, although the average value within an element is representative. For this reason, it is necessary to utilise a smoothed version of the rotation field using the now standard approach

$$\tilde{\psi} - c_\psi \nabla^2 \tilde{\psi} = \psi \tag{37}$$

where the parameter $c_\psi = \frac{1}{2} l_\psi^2$, where l_ψ defines the smoothing length for the rotation field. The perturbation is fairly localised within each element, and hence the smoothing length is taken to be small, such that $l_\psi = h$. The second consideration is that a sharp switching criteria can cause numerical problems, i.e. $\chi = (\tilde{\psi} > 0)$ is either 0 or 1. A sharp approach proves to be effective for geometries where there is a high initial stress concentration feature, such as a crack, where the stress field makes the direction of damage growth clear from the start. In this case damage quickly initiates locally and dominates the response. However, if the stress concentrator is fairly weak, such as the circular hole in this example, it is possible for damage to initiate on a more global basis, far from the hole, where the rotation is very small and hence the switch is unstable, leading to strong differences in behaviour between adjacent elements that are exacerbated as further damage accumulates. To prevent this χ is defined to be a smooth, continuous function

$$\chi = \frac{1}{2}\left[1 + q\left(\frac{\tilde{\psi}}{\Delta\psi}\right)\right] \tag{38}$$

where $q(x)$ is a smoothed sign function, shown in Figure 8, and $\Delta\psi$ is the width of the angular transition. It is found that a value of $\Delta\psi = 2\gamma_0$ works well for the local model, but that a tighter transition is necessary for the non-local model, with a value of $\Delta\psi = 0.2\gamma_0$. For the same reasons, it is found that the measure $sign(\tau_b)$ in equation (34) is not a reliable measure around the damage zone. This could also be treated as above, but in practice the sign of the shear stress on each failure system is known in advance in these simple monotonic loading problems, and hence it is just prescribed. Note also that the value of χ is often not clearly defined away from the damage zone (i.e. $\chi \approx 0.5$) which means that a well-defined, tight damage zone is necessary. This has profound effects for the non-local model, as a large smoothing length results in a broad, highly diffuse damage zone, the edges of which can quickly start to erroneously propagate parallel to the failure plane normal, $\underline{n}^{(+)}$. To avoid this it is necessary to choose a small smoothing length, related to the mesh size. As stated previously, a small mesh-dependent value of $l_\gamma = \frac{h_{\max}}{4}$ is found to work very well. This has similarities with gradient-enhanced damage models [30,56] where the smoothing length approaches the distance between Gauss points in regions of interest (i.e. high damage) although here the smoothing length takes this small value at all points.

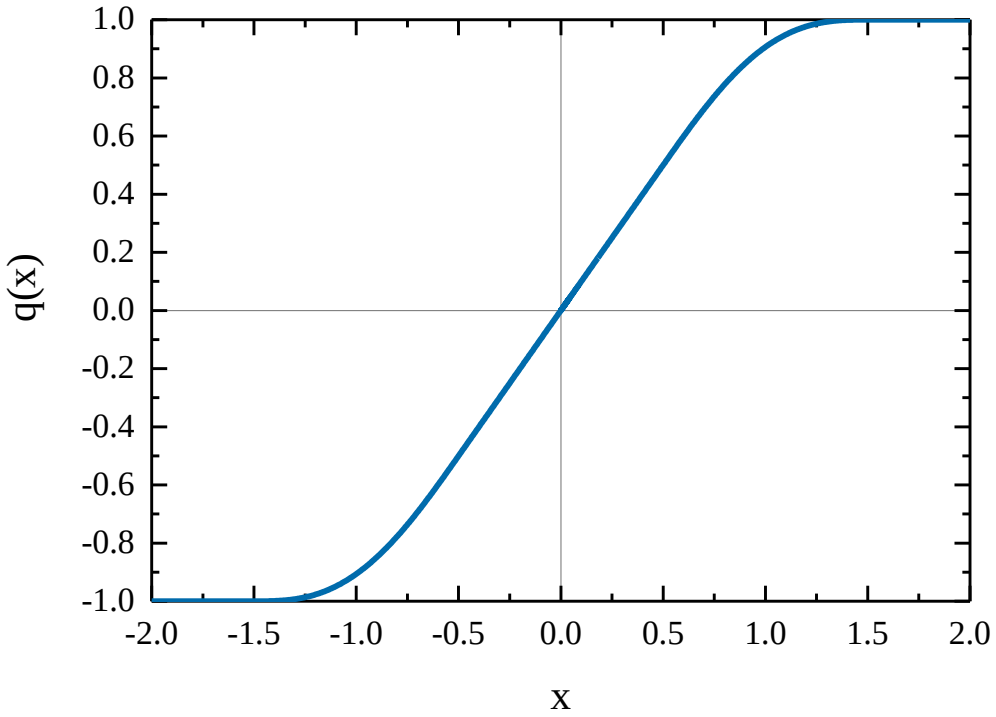

Figure 8: The smoothed sign function $q(x)$ used in the failure plane selector of equation (38). The linear ramp function has a gradient of one with a smoothed transition to the horizontal of radius 0.5.

The current aim is to only activate the first failure system, $(+)$, whilst suppressing erroneous damage growth normal to it. To do this the strain measure of equations (9) and (10) are replaced by $\kappa = \chi\gamma_{eq}$ for the local model and $\kappa = \chi\tilde{\gamma}_{eq}$ for the non-local model. This zeroes the equivalent strain when failure system $(-)$ is deemed active, effectively turning it off. Similarly, the $(-)$ system can be activated and the $(+)$ system suppressed if the strain measure $\kappa = (1-\chi)\gamma_{eq}$ is used. Results for the local and non-local models are shown in Figures 9 and 10 respectively. When compared to Figures 6 and 7, it is clear that equation (38) is effective in suppressing erroneous damage growth. The values of χ and $\tilde{\psi} > 0$ are illustrated alongside the damage field for reference. In Figure 9a, the local model exhibits a narrower crack than the equivalent crack determined with the non-local model in Figure 10a. Figure 9c shows that failure plane $(+)$ is active ($\chi = 1$) where the crack exists and inactive ($\chi = 0$) where the anomalous growth normal to the plane occurred in Figure 6a. This can also be seen in the rotation field $\tilde{\psi} > 0$ in Figure 9b. The crack eventually cleaves the sample in Figure 9d. In the local model, the crack widens as the element size increases away from the hole, as its width is determined by the local mesh size. The damage profile is slightly rougher than that for the smoothed non-local model as one would expect. There is minor smearing of the damage at the end of the final cleavage cracks, as the stress at the crack tip interacts with the free surface as it is approached. However, the region of intense damage, where the majority of shearing takes place, is well-defined. The non-local model, shown in Figure 10a and 10d, propagates as a smoother, slightly less distinct, crack. The advantage of this approach is that the damage zone is smooth and independent of the mesh size, leading to a final crack of constant width. The failure plane selector, χ, is therefore also less distinct, as shown in Figures 10c and 10f, as well as the sign of the rotation $\tilde{\psi} > 0$, shown in Figures 10b and 10e.

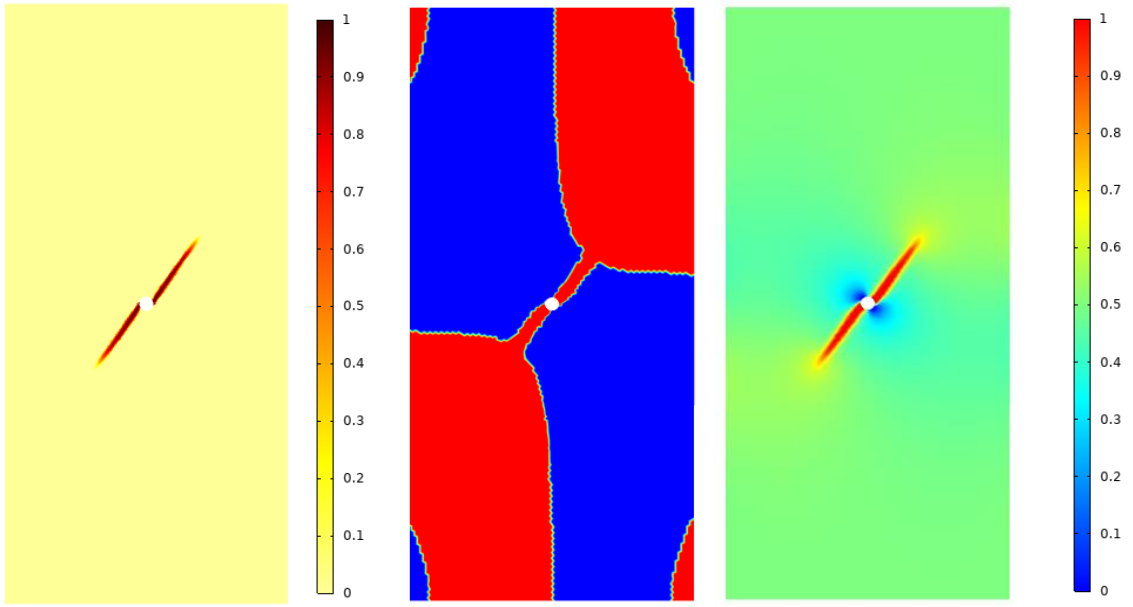

(a) (b) (c)

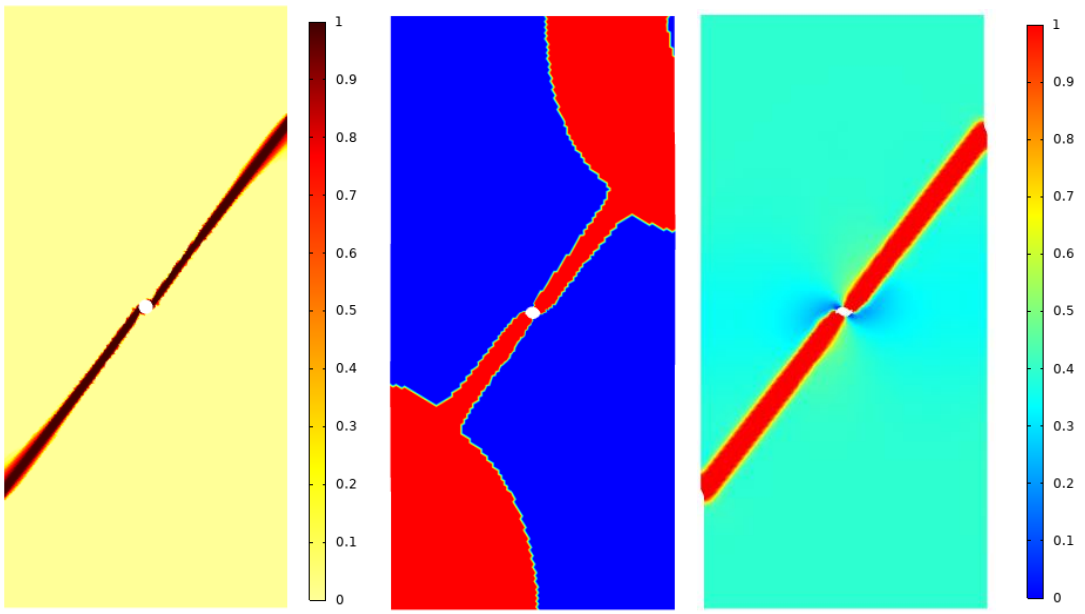

(d) (e) (f)

Figure 9: Uniaxial compression test using the local model with a single active failure plane with normal crack growth suppression using equation (38). In early stages when $\delta = 0.69mm$ (a) damage w, (b) rotation direction ($\psi > 0$) and (c) active plane selector χ, and after cleavage at $\delta = 0.72mm$ (d) damage w, (e) rotation direction ($\psi > 0$) and (f) active plane selector χ.

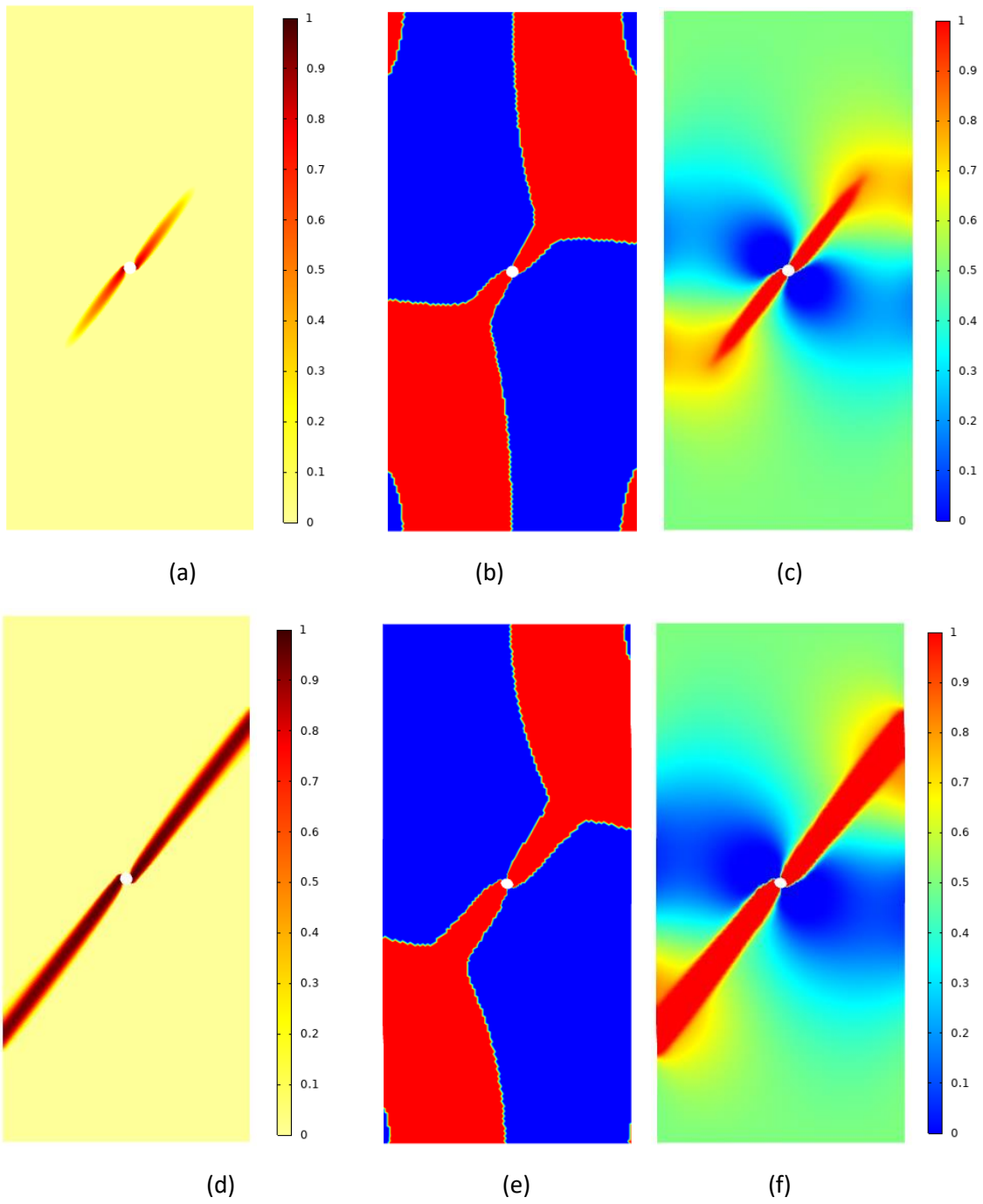

Figure 10: Uniaxial compression test using the non-local model with a single active failure plane with normal crack growth suppression using equation (38). In early stages at $\delta = 0.6mm$ (a) damage w, (b) rotation direction ($\psi > 0$) and (c) active plane selector χ, and after cleavageat $\delta = 0.65mm$ (d) damage w, (e) rotation direction ($\psi > 0$) and (f) active plane selector χ.

Effect of the friction angle ϕ

The single plane failure model is clearly suppressing anomalous growth normal to the plane as intended. Figure 11 shows that it is also reproducing the expected friction angle $\theta = 45^o - \frac{\phi}{2}$ from the vertical (direction of maximum compressive stress). This is tested for the non-local model, where the final cleavage damage states for the three cases of $\phi = 0^o, 15^0$ and 30^o are shown, along with the associated displacement and deformed shapes. The results for the local model are similar. The displacement profiles demonstrate a narrow shear band, with the majority of the shear strain accommodated within a band just one element wide. The expected orientation of the failure planes is clearly reproduced as required, as indicated by the angles inset on the plots. As discussed in section 3, the anisotropic elasticity model of equations (2) and (29) are responsible for correctly aligning the crack.

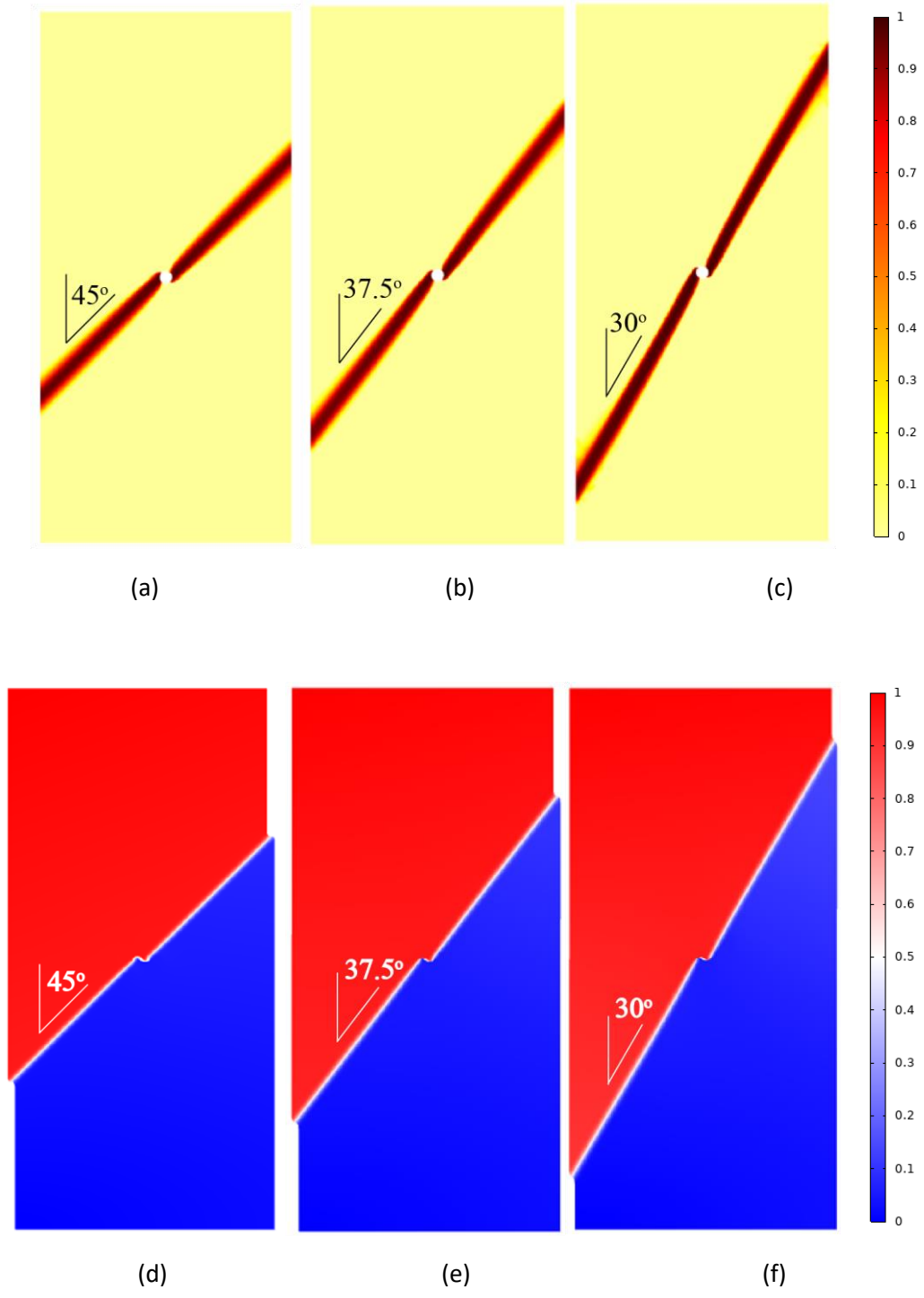

Figure 11: Uniaxial compression test using the non-local model with a single active failure plane with normal crack growth suppression using (38) for exponential softening: damage w for (a) $\phi = 0^o$, (b) $\phi = 15^o$ and (c) $\phi = 30^o$ and normalised displacement u_{TOT}/δ with deformed shape for (d) $\phi = 0^o$, (e) $\phi = 15^o$ and (f) $\phi = 30^o$.

Mesh-size independence

The force-displacement plots for the non-local model of Figure 11 are shown in Figure 12a, for mesh sizes of $h_{\max} = 1mm$ (solid lines) and $h_{\max} = 2mm$ (dashed lines). The force reaches a well-defined peak, where damage initiates and rapidly grows causing the force to drop quickly. The solid and dashed lines are similar indicating that the model is largely independent of the mesh size. The main difference between the two mesh sizes is the residual friction that remains after full cleavage has been achieved. Physically the force should drop to zero in this case, however it can be seen that a not insubstantial force remains. This is not unexpected, as Figure 4a showed that a residual force remains for a narrow crack band, as achieved here. The case of uniaxial compression, with zero residual friction, proves to be the worse case scenario in this respect. A small residual friction allows for a higher stress to be sustained normal to the crack face, which in turn increases the friction and so on. Hence a very small residual friction force can lead to a substantial force post-cleavage. It is found that just a 0.6% increase in the damage shear stress τ_b can remove the frictional force entirely. Fortunately, as will be shown later, the frictional force is much closer to the expected value for the case where the friction is not expected to be zero. Similar results for the local model are shown in Figure 12b. The force-displacement curves follow a similar trend to those seen in Figure 12a, although the peak force is a bit higher, and drops more rapidly after this. There is a more noticeable difference between the results for the two mesh sizes, which is to be expected as this is a known weakness of the local model. It should be noted that in all cases the residual force post-cleavage reduces as the deformation continues. As shown in Figure 4a, for the given elasticity model, this reduction in the residual force must be accommodated by a widening of the crack. In Figure 12a it can be seen that the percentage residual force is between 2-5% when $\delta = 2mm$.

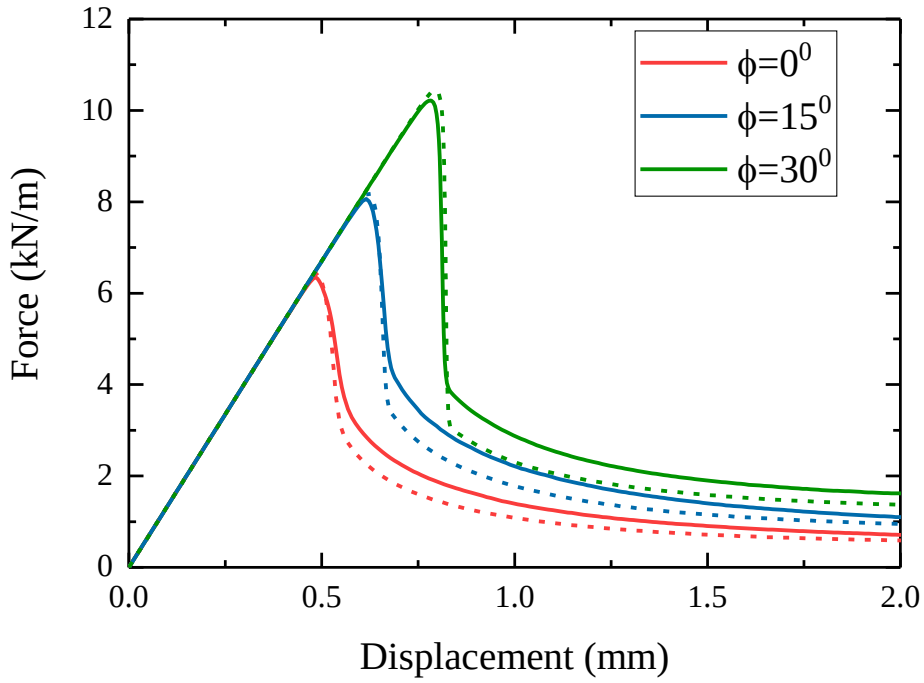

(a)

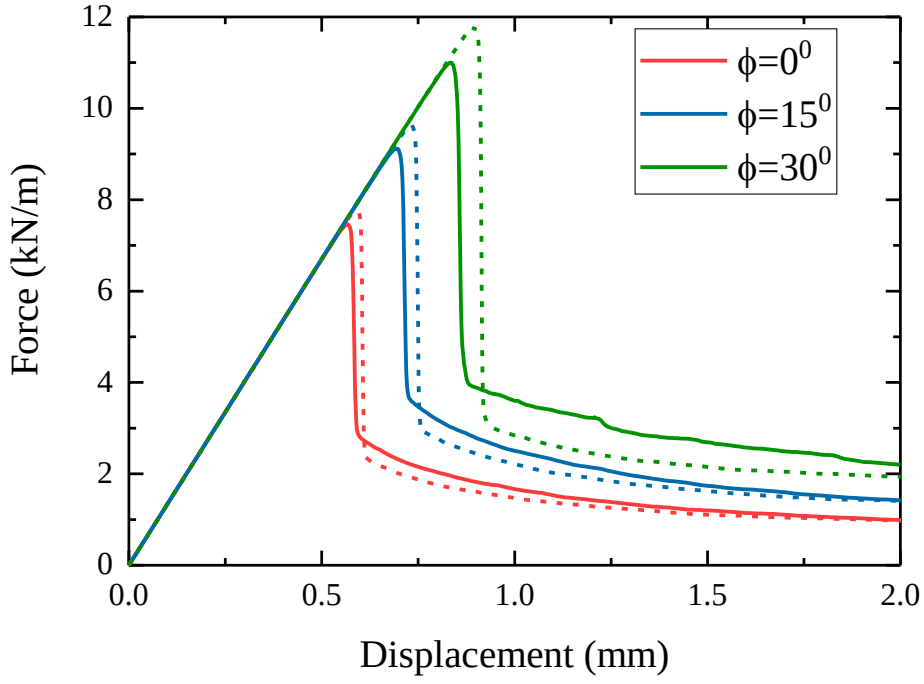

(b)

Figure 12: Force-displacement curves for the uniaxial compression tests for different friction angles $\phi = 0^o, 15^o$ and 30^o for (a) non-local and (b) local models. The dashed lines are for a mesh size of 2mm and the solid lines are for a mesh size of 1mm.

Effect of confining pressure, p_c

Most geological samples are tested in a biaxial compression state, subject to a fixed horizontal confining pressure p_c, which induces a non-zero frictional force on the crack face. In the fully cleaved state, the equivalent strain must be zero in the damage zone, i.e. the material has no remaining cohesive strength so $\gamma_{eq} = \gamma_0 = 0$. Taking into account the cross-sectional area reduction due to the hole, the resulting friction stress on the crack face can then be calculated for comparison with the numerical results. Figure 13 shows the force-displacement responses for different confining pressures of $p_c = 0, 25, 50$ and $75\ kPa$ for two different mesh sizes. The expected residual friction force on the crack face is indicated in each case by the black horizontal dashed lines on the right hand side. It is clear that the results are reasonably mesh independent. The deviation from the predicted friction force is greatest when there is no confining pressure ($p_c = 0$), for which the expected value is zero, although it is observed that the force is still decreasing at the end of the simulation. The deviation decreases as the confining pressure increases, with no noticeable difference at the highest confining pressure ($p_c = 75\ kPa$). In this model, the Pressure Formulation was used to solve the elasticity problem, which gives a slightly enhanced convergence towards the calculated friction force.

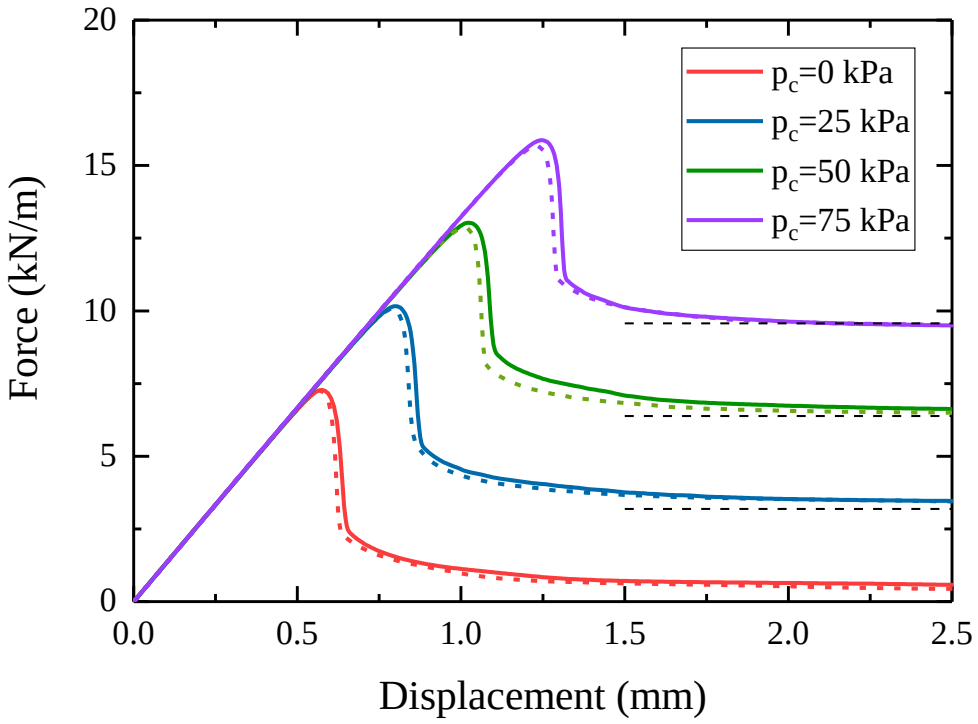

Figure 13: The effect of confining pressure p_C on the force-displacement response for the non-local model. The solid lines are for a mesh size of 1mm and the dashed lines for a mesh size of 2mm. The horizontal black dashed lines on the right indicate the expected asymptotic residual friction force at the given confining pressure.

Effect of shear fracture energy, G_{II}

A shear fracture energy of $G_{II} = 30\,J/m^2$ has been assumed so far. Here the consequences of assuming a lower value of $G_{II} = 3\,J/m^2$ are investigated. This reduces the value of γ_c from 25.2% to 2.7%, and therefore $\beta_{\exp}$ goes from 62 to 5.8. The force-displacement responses for the local (dashed lines) and non-local (solid lines) models can be seen in Figure 14a for the case of zero confinement pressure. In this case the residual friction force is expected to asymptote towards zero post-failure. The local and non-local models give similar responses, with a higher peak force for the non-local model as smoothing always reduces the peak strain value. The reduction in the shear fracture energy has a strong effect, with fracture occurring much earlier with the lower value, even though the damage initiation strain $\gamma_0 = 0.4\%$ is unchanged. This demonstrates that the damage takes some time to grow and affect the force-displacement curve for the higher fracture energy of $30\,J/m^2$. For the lower fracture energy, the crack grows quickly after initiation, with a very rapid drop off in the force indicative of fast fracture in a more brittle material. Figure 14b investigates the change in response when there is a confining pressure of $p_c = 25\ kPa$. The results are as expected, with a lower fracture energy causing an earlier and sharper transition at the failure load. The residual force also converges quickly and accurately towards the analytically calculated residual friction force. In this case the solid and dashed lines show the different responses for the linear (solid) and exponential (dashed) strain softening models of equations (5) and (7) respectively. The difference is relatively small, but the linear softening model causes post-peak damage to grow less quickly than the exponential model initially, but then more rapidly in the later stages, as one would expect from comparison of the stress-strain relationships for the two models in Figure 1. The residual friction is lower for the linear model as this actually achieves the fully damaged state ($w = 1$ at $\gamma = \gamma_f$) whereas the exponential model only asymptotes towards full damage.

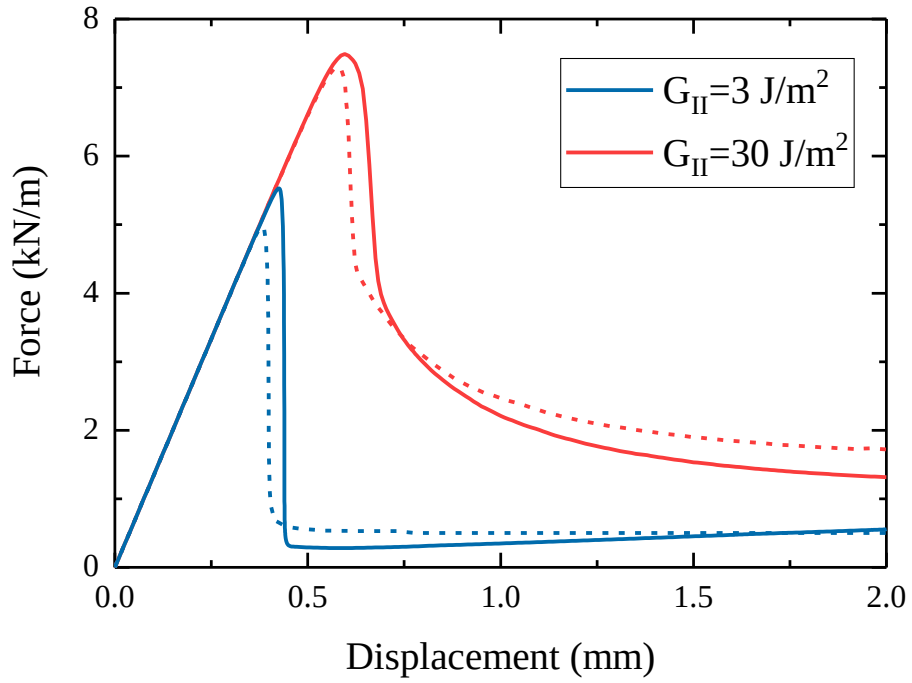

(a)

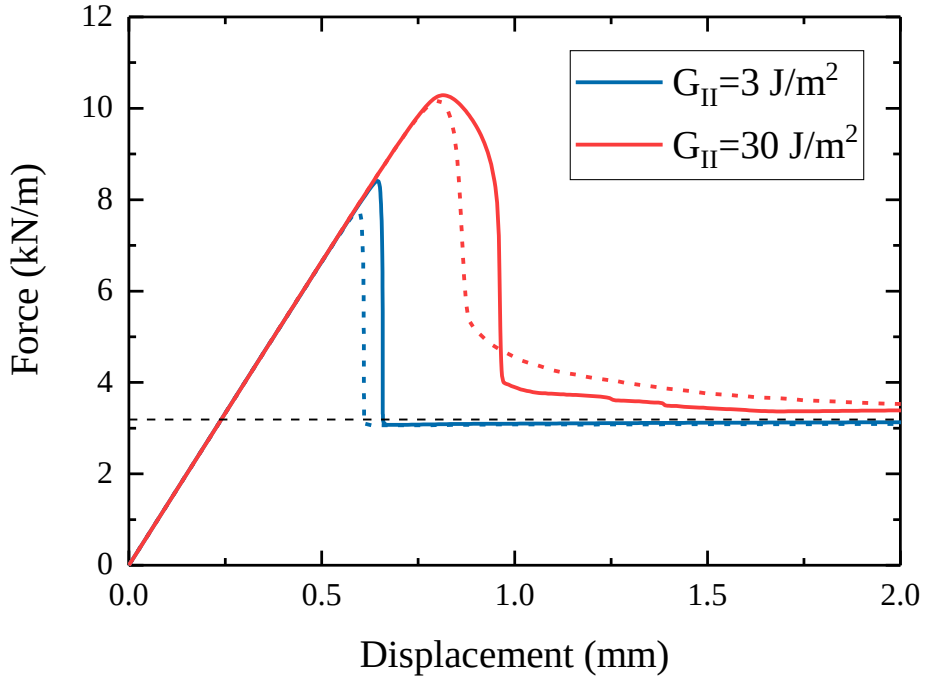

(b)

Figure 14: The effect of fracture energy G_{II} on the force-displacement response. (a) $p_c = 0\ kPa$ for the local (dashed) and non-local (solid) models. (b) $p_c = 25\ kPa$ for the linear (solid) and

exponential (dashed) strain softening models of equations (5) and (7) respectively. The horizontal black dashed line is the expected residual friction force.

4.2 Dual failure plane tests

In the previous section, only the $(+)$ failure plane was activated. In theory, both of the failure planes are equally likely to be active. However, if fracture is rapid, then one may fail before the other becomes active, and in practice there will always be some asymmetry that favours the activation of one before the other. In this section the effect of having both failure planes active simultaneously is investigated. This is simply achieved by reverting to the original form of the strain measure, i.e. $\kappa = \gamma_{eq}$ for the local model etc, but with the implementation of the plane selector χ of equation (38). Interestingly, in this case the Pressure Formulation could not be used as it proved to be highly unstable, generating oscillations in the damage field. Figure 15 shows the results for the local model. In Figure 15a damage evolves equally on both failure systems to produce four similar cracks in this symmetric setup. In Figure 15b it can be seen that a small perturbation in the symmetry favours the formation of a dominant crack in one direction, probably due to slight asymmetries in the mesh. The final cleavage state is shown in Figure 15c, indicating that the primary crack forms along the $(-)$ plane and the secondary crack on the $(+)$ system has no effect on the deformation mode. The comparable results for the non-local model are shown in Figure 16. In this case the simulation found it impossible to break the initial symmetry, and failed to solve beyond the state shown. This is a unique feature of this particular problem, where both failure planes are equally favoured, and is not expected to be restrictive on its wider use.

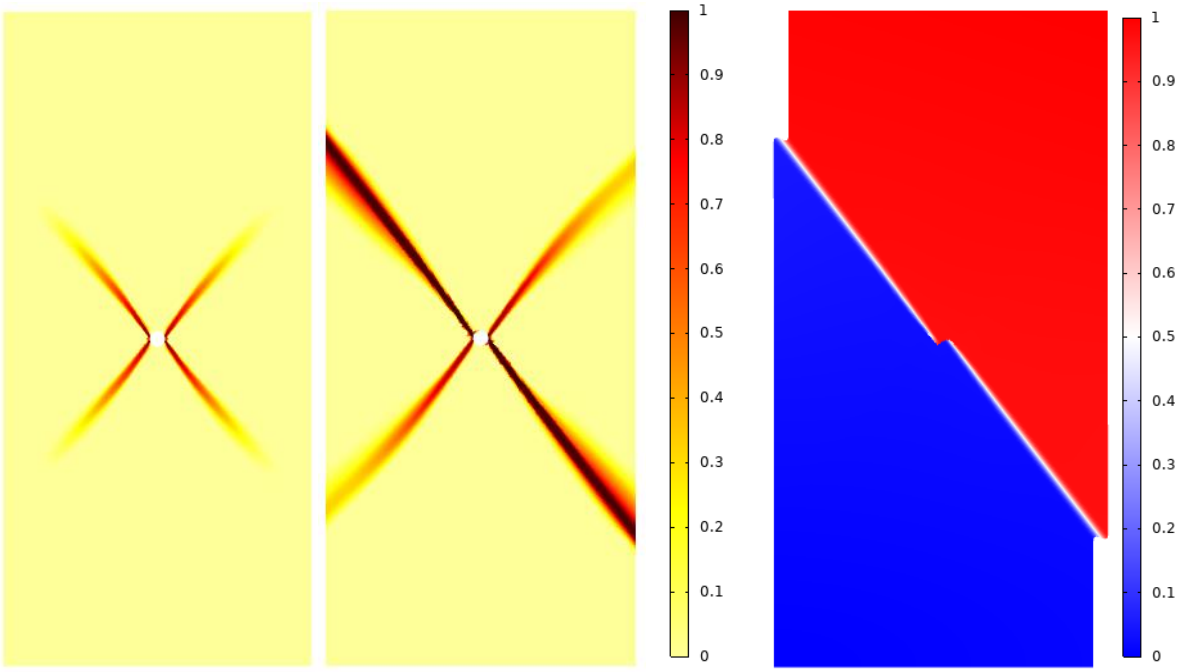

(a) (b) (c)

Figure 15: Uniaxial compression test with both failure planes active using the local model with $\phi = 15^o$ and $h = 1mm$ showing the damage level at (a) $\delta = 0.6mm$ and (b) $\delta = 0.65mm$ and (c) the associated normalised total displacement u_{TOT}/δ.

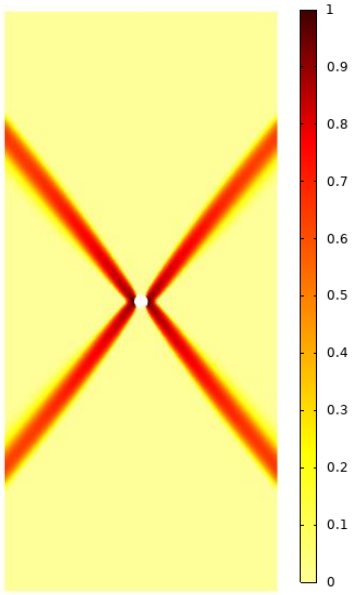

Figure 16: Uniaxial compression test with both failure planes active using the non-local model with $\phi = 15^o$ and $h = 1mm$ showing the damage level at $\delta = 0.65mm$. The simulation did not progress further.

The effect of problem symmetry is clearly an issue for the non-local model when both failure planes can become active. Hence the symmetry of the problem is broken by replacing the 2mm radius circular hole with an elliptical hole with a horizontal major axis of 4mm and a vertical minor axis of 1mm. The central hole is then rotated anti-clockwise 10° about its centre. The results for the local and non-local models are shown in Figures 17 and 18 respectively. In both cases, the effect of high ($30\ J/m^2$) and low ($3\ J/m^2$) shear fracture energy are investigated. In Figure 17a, the local model generates a dominant crack on the anticipated $(+)$ failure plane which is favoured by the orientation of the elliptical hole. The secondary cracking in the $(-)$ failure plane is slightly reduced from that seen in Figure 15b. It is interesting to see that secondary cracking is absent in the lower fracture energy case of Figure 17b. It is clear that this allows damage to progress much faster once initiated, such that cracking on the secondary failure system does not have the opportunity to develop. This is also seen for the non-local model in Figure 18. The asymmetric hole now generates a dominant crack for the case of Figure 18a, compared to the failure to achieve this in the comparable symmetric case of Figure 16. However, the crack is in the unexpected $(-)$ failure orientation, contrary to the dominant crack seen for the local model in Figure 17a. The secondary cracks are much more established that for the local model case. Fortunately the lower fracture energy case in Figure 18b produces a response very similar to that seen for the local model in Figure 17b, where there is no secondary cracking, and the dominant crack appears in the $(+)$ system. The conclusion is that activating both failure systems in a very soft material system can lead to substantial cracking on both systems. For a stiffer (more brittle) material the response is likely to only activate one of the failure planes.

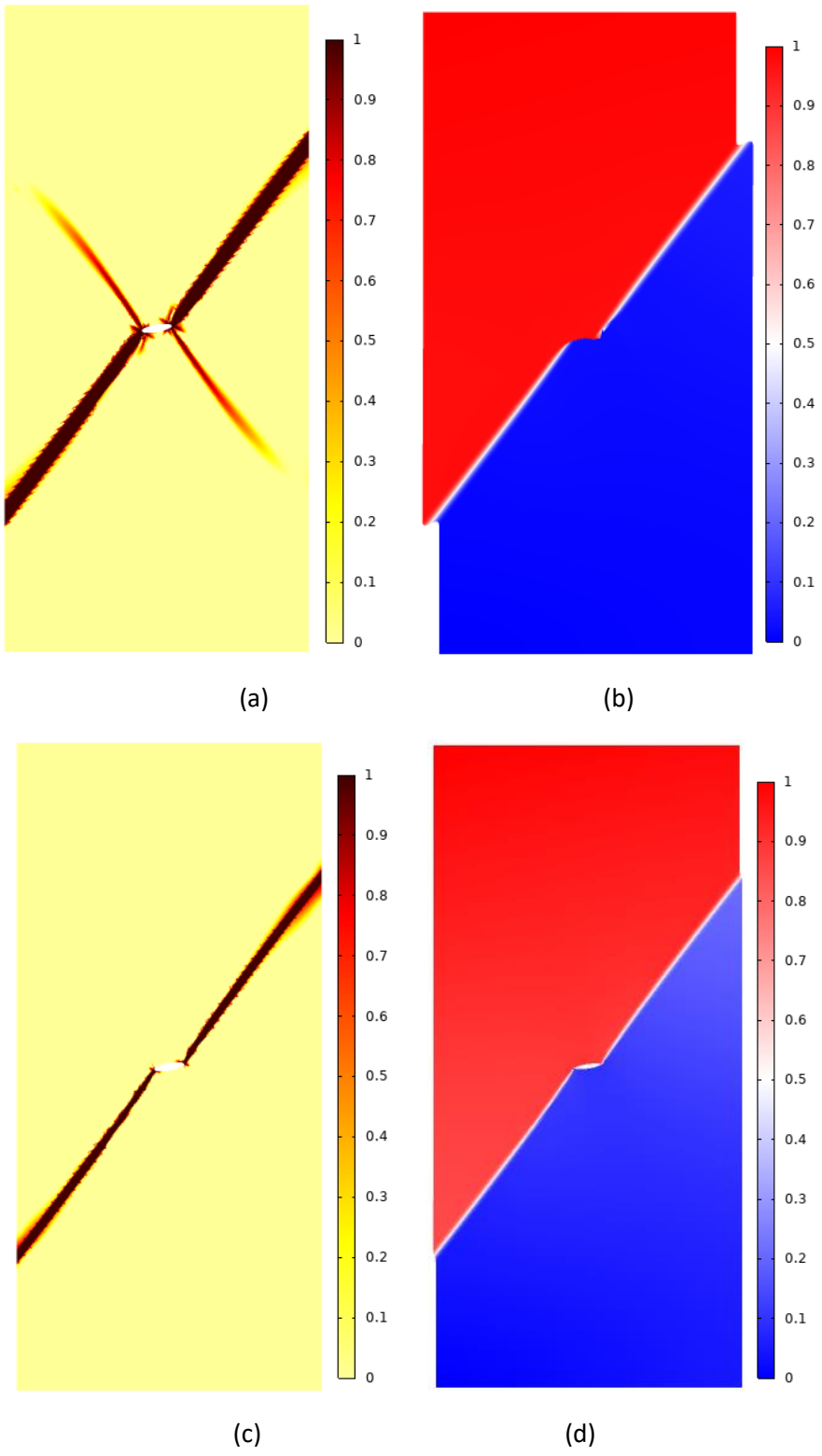

Figure 17: Uniaxial compression test for an asymmetric hole with both failure planes active using the local model with $\phi = 15^o$ and $h = 1mm$ showing the damage level and normalised displacement u_{TOT}/δ for (a) and (b) at $\delta = 2mm$ for $G_{II} = 30\,J/m^2$ and for (c) and (d) at $\delta = 0.4mm$ for $G_{II} = 3\,J/m^2$.

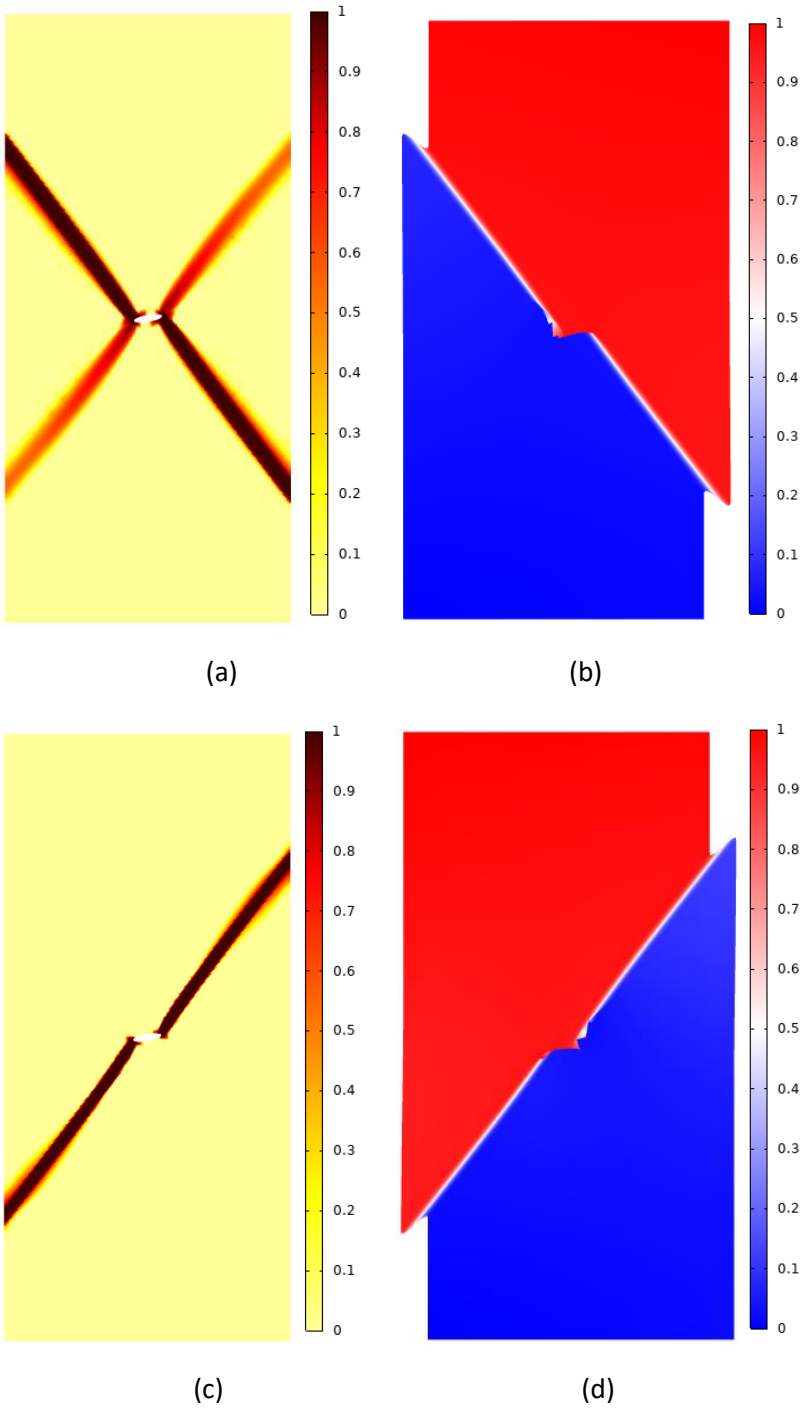

Figure 18: Uniaxial compression test for an asymmetric hole with both failure planes active using the non-local model with $\phi = 15^o$ and $h = 1mm$ showing the damage level and normalised displacement u_{TOT}/δ for (a) and (b) at $\delta = 2mm$ for $G_{II} = 30\ J/m^2$ and for (c) and (d) at $\delta = 0.4mm$ for $G_{II} = 3\ J/m^2$.

Slope test

For comparative purposes, we initially follow Regueiro and Borja [57], and subsequently Fei and Choo [34], in modelling the failure of a 45° slope. As indicated by those authors, this does not claim to be a physically relevant study for the parameters used, which are for an overconsolidated clay. A 45° slope is constructed, as shown in Figure 19, such that the lower horizontal section is $H + 10m$ wide, the upper horizontal is 10m wide, and the slope has a vertical height of H. For the initial comparative analysis $H = 10m$. A displacement is applied at the central point of a 4m wide and 1m tall rigid foundation at the top of the slope. The vertical boundary is on rollers and the bottom horizontal boundary is fixed. Only the $(+)$ failure plane is activated, with χ defined by equation (38) and $\kappa = \chi\gamma_{eq}$ for the local model and $\kappa = \chi\tilde{\gamma}_{eq}$ for the non-local model. The material properties [34] are: a low cohesive strength of $C = 40\ kPa$, peak friction angle of $\phi = 16.7^o$, a residual friction angle of $\phi_r = 10^o$, a plane strain Young's modulus of $\frac{E}{1-\nu^2} = 10\ MPa$, a Poisson's ratio of $\nu = 0.4$ and a mass density of $\rho = 2040\ kg/m^3$. The applied displacement is enforced at a rate of $0.3m/s$. Regueiro and Borja [57] use a Drucker-Prager plasticity model which does not depend on the definition of a fracture energy. Fei and Choo [34] adopt a large (but not unreasonable [55]) fracture energy of $G_{II} = 10\ kJ/m^2$ for comparison with the results of Regueiro and Borja. The effect of this parameter is investigated here. The above values set the onset of failure at $\gamma_0 = 1.3\%$. A very coarse, unstructured triangular mesh is chosen initially, with $h_{\max} = 0.35m$. This gives a critical failure strain of $\gamma_c = 24\%$ and a value of $\beta_{\exp} = 17.4$. The Pressure Formulation is used in all cases. The only affect this has on the final result is a slight reduction in any unphysical residual friction, as expected from Figure 4a.

5.1 Comparative study

Following the previous studies [33,57], gravity is applied and then the displacement reset to zero. This zeroing is done by applying a volumetric body force (load contribution only) equal but opposite to the stress induced by the gravitational load. This may appear to have no effect, but it does as this stress remains active on the damaged failure plane, ensuring that the force applied to the foundation asymptotes towards zero after failure has occurred, as seen in the model of Fei and Choo [34]. This assumption is revisited in the next sub-section. Figure 20 shows the damage state and the displacement field for the local model. These coarse simulations took about 4 minutes each to complete on a Pentium i9 3.6GHz dual processor core. The images are not as attractive as those produced with a fine mesh, but it demonstrates the efficiency of the method in producing useful results at relatively low cost and suggests that implementation in 3D is computationally realistic. The failure path in all cases is very similar to those produced in previous studies [34,57]. As shown in Figure 20a, the crack initially propagates at a width of just one element wide and then, as seen in Figure 20b, it broadens behind the crack tip over time as a mechanism for reducing the erroneous friction contributions predicted by Figure 4a. The underlying mesh can be clearly seen in the results, as one would expect for a local model, but it is impressive that the crack still manages to propagate through the mesh along a smooth trajectory. The deformed shape and displacement field are smooth with the typical very narrow band of intense shear. Its path is slightly lower than that seen in Figure 21 for the non-local model. The damage zone for the non-local model is broader (4-5 elements wide) but much less mesh-influenced than seen in the local model, as expected. The associated force-displacement curves are illustrated in Figure 22 and compared with the results for previous studies [33,57]. The two curves for the local and non-local models with a shear fracture energy of $G_{II} = 10\ kJ/m^2$ have a roughly similarly breaking point to those observed by Regueiro and Borja [57] and Fei and Choo [34]. As in those studies, failure does not occur at the damage instigation point, as the force continues to

rise as the crack extends through the body until a critical peak point is reached. This peak force occurs a little later for this model than the previous models [34,57] for this value for the fracture energy. The local model shows a slightly stepped rise and decay in the force during failure. This is likely due to the damage propagating more readily along beneficially aligned elements at certain stages, as is commonly observed in tensile crack band models. These stages can be observed in Figure 20a where the damage propagates as a thinner crack around the mid-point of the failure interface. The residual frictional force is also higher for the local model as the final crack in Figure 20b has not widened as effectively as that for the non-local model in Figure 21b.

The effect of the shear fracture energy G_{II} is explored further with the non-local model in Figure 22. As seen in Figure 14, a reduction in the fracture energy is expected to lead to more rapid extension of a nascent crack, and this is the case here also, where there is a strong decrease in the peak force and a clear increase in the force drop off rate thereafter as the fracture energy is reduced. For $G_{II} = 3\ kJ/m^2$ the onset of non-linearity in the force-displacement curve coincides with the peak force. For $G_{II} = 1\ kJ/m^2$ the force has two peaks, with a second rise required to complete the fracture process. For $G_{II} = 0.1\ kJ/m^2$ the peak force is at its lowest and the fracture process is truly brittle, i.e. very rapid. All the simulations are for a coarse mesh of $h_{\max} = 0.35m$ spanning a range of $\beta_{\exp} = 17.4$ for $G_{II} = 10\ kJ/m^2$ to $\beta_{\exp} = 1.28$ for $G_{II} = 1\ kJ/m^2$. A further reduction in G_{II} requires a reduction in the mesh size to keep $\beta_{\exp} > 1$. Hence the curve for $G_{II} = 0.1\ kJ/m^2$ uses a much finer mesh of $h_{\max} = 0.035$ which retains the value of $\beta_{\exp} = 1.28$. This also has the benefit of producing a more attractive damage plot, which is shown in Figure 23. It can be seen more clearly here that the crack propagates as a fully damaged zone, with the stress relief behind the crack influencing the path of the crack ahead. In this respect the path may be expected to be slightly different to that obtained in previous studies [34,57].

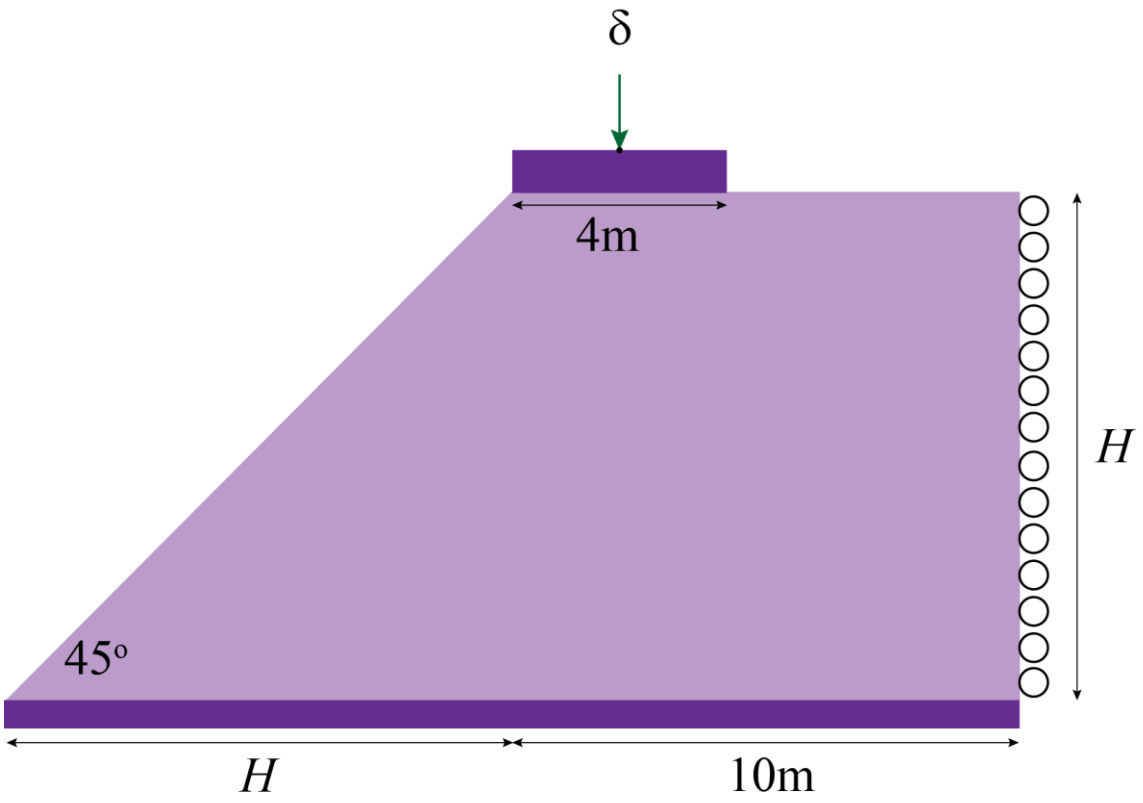

Figure 19: Schematic drawing of the slope test. The dark purple areas are rigid. A 4m section of the top plateau is destabilised by the action of a point displacement δ at the centre of the rigid block, which is free to rotate. The height of the slope H can be adjusted but the slope remains at 45°. The vertical boundary is on rollers and the bottom horizontal boundary is fixed.

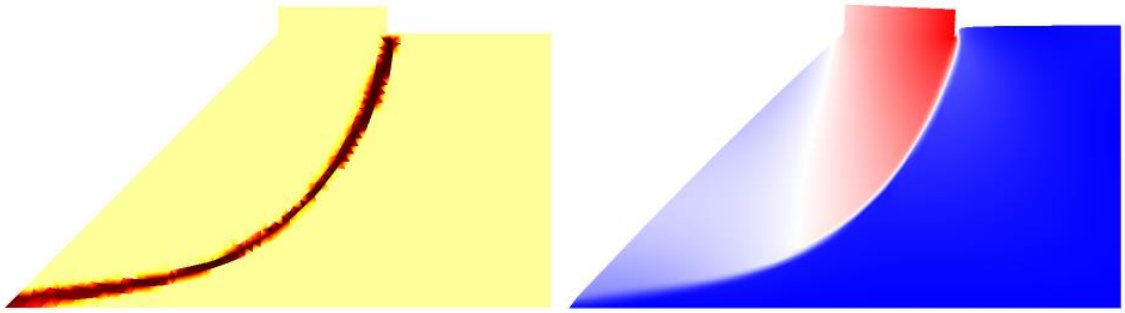

(a)

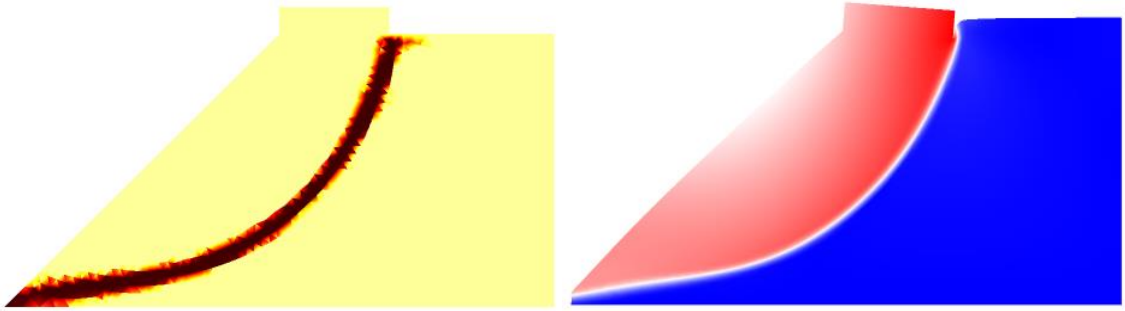

(b)

Figure 20: Slope failure analysis using the local model with $H = 10m$, $h_{\max} = 0.35m$, $C = 40kPa$ and $G_{II} = 10\ kJ/m^2$ showing damage (left image) and associated displacement field and deformed shape (right image) at (a) $\delta = 0.17\ m$ and $(b)\ \delta = 0.3$m.

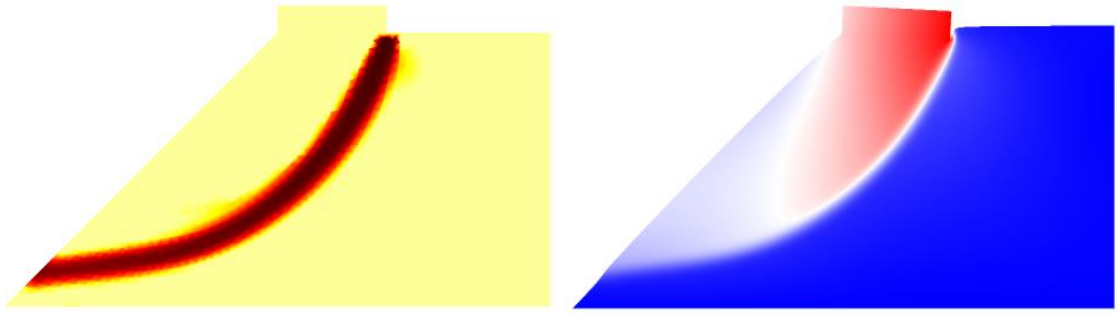

(a)

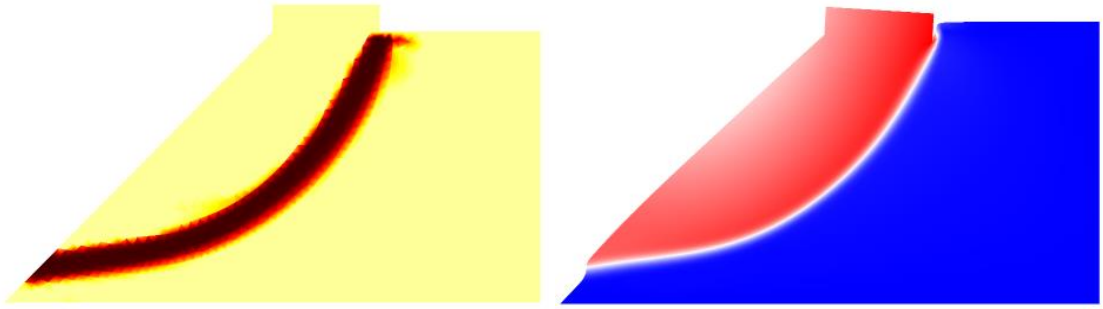

(b)

Figure 21: Slope failure analysis using the non-local model with $H = 10m$, $h_{\max} = 0.35m$, $C = 40kPa$ and $G_{II} = 10\ kJ/m^2$ showing damage (left image) and associated displacement field and deformed shape (right image) at (a) $\delta = 0.19\ m$ and (b) $\delta = 0.3$m.

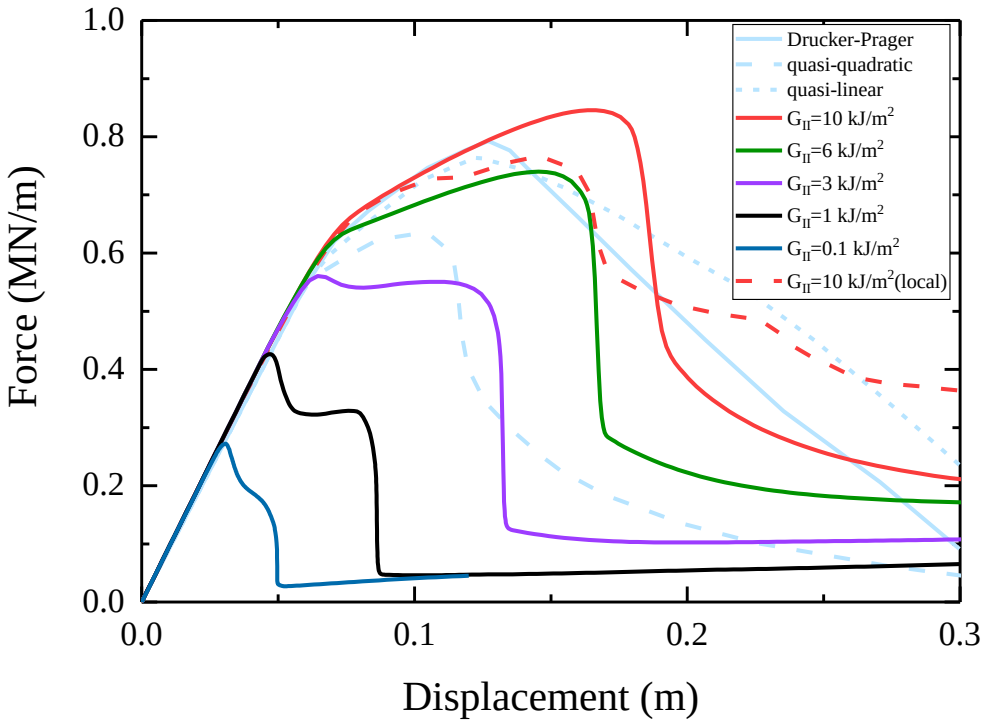

Figure 22: Force-displacement curves for the slope analysis with $H = 10m$, $h_{\max} = 0.35$ and $C = 40\ kPa$. The previous results of Regueiro and Borja [57] (Drucker-Prager) and Fei and Choo [34] (quasi-linear and quasi-quadratic) are shown in light blue. Results for the non-local model are shown for various values of the shear fracture energy G_{II}, with $G_{II} = 10\ kJ/m^2$ corresponding to Figure 21, and $G_{II} = 0.1\ kJ/m^2$ corresponding to Figure 23. The result for the local model of Figure 20 is also shown.

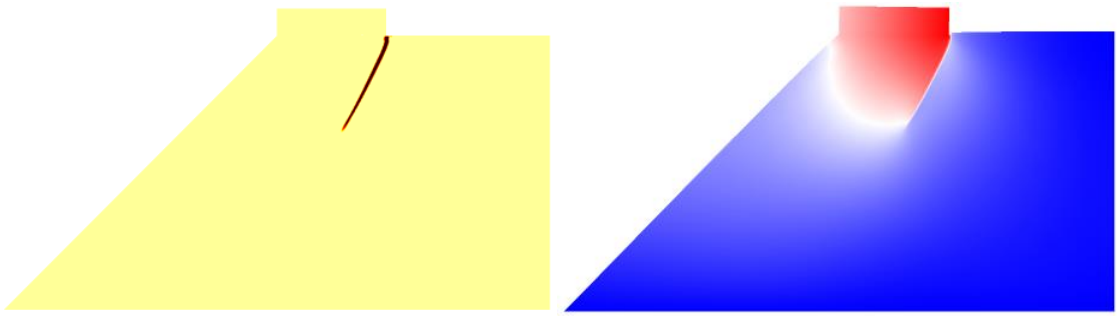

(a)

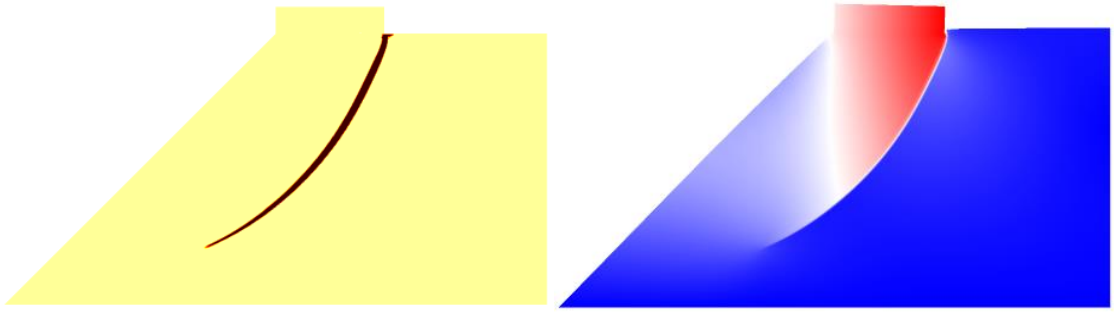

(b)

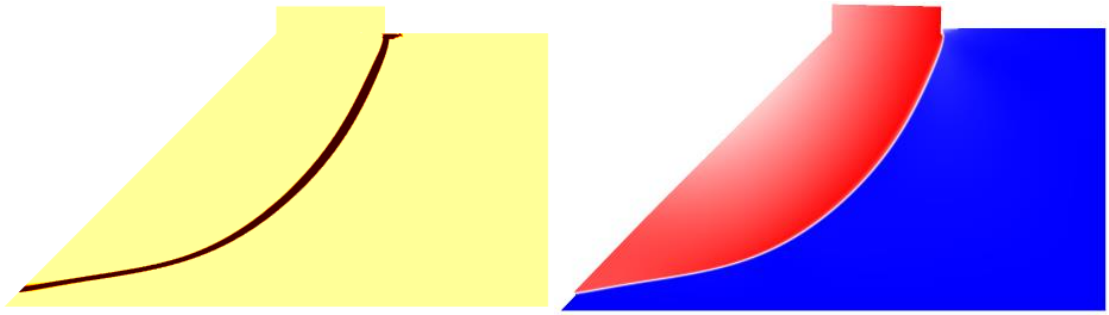

(c)

Figure 23: Slope failure analysis using the non-local model with $H = 10m$, $h_{\max} = 0.035m$, $C = 40kPa$ and $G_{II} = 100\ J/m^2$ showing damage (left image) and associated displacement field and deformed shape (right image) at (a) $\delta = 0.033\ m$, $(b)\ \delta = 0.042m$, and (c) $\delta = 0.051m$.

5.2 Study with active gravity

The stress state within a soil or clay can change over time due to compaction and creep leaving just a residual hydrostatic stress state. This roughly parallels the assumption of neglecting the displacement field due to gravity in the previous study. However, this is not expected to be the case for some geological materials, such as igneous rocks, e.g. granite. It is therefore of interest to conclude investigation of the slope failure problem when the forces and displacement field due to gravity are not zeroed prior to commencement of the damage simulation. The first observation in this case is that gravitational forces induce a stress concentration at the triangular corner at the bottom of the slope. This causes failure to initiate at this lower corner, as seen in some other studies [58]. This is because the cohesive strength of the material, $C = 40\ kPa$, so too low to support its own weight in this scenario. As such the cohesive strength is increased, but only to $C = 80\ kPa$, to keep it as close to the original value as possible. There are now two competing forces acting on the slope, the applied load and the gravitational field. The slip path predicted by the latter is steeper than the shallow path seen in Figure 23. As gravity dominates at the start, the initial failure trajectory is steeper than before. As such the height of the slope is increased to $H = 20m$. A finer mesh size of $h_{\max} = 0.035m$ is used, but the other values are kept the same. This gives $\beta_{\exp} = 88$ for the largest shear fracture energy value of $G_{II} = 10\ kJ/m^2$ and a value of $\beta_{\exp} = 8.4$ for the smallest value of $G_{II} = 1\ kJ/m^2$. A result for the non-local model for $G_{II} = 1\ kJ/m^2$ is shown in Figure 24 at different stages in the loading. The displacement field shown is relative to the initial configuration, i.e. with gravity but without an applied load. The associated force-displacement curves are shown for a range of shear fracture energies in Figure 25. Failure of the slope is fairly rapid after the peak force is reached. This peak force reduces as the shear fracture energy is reduced. A key point of interest is that the applied force becomes negative (tensile) post-failure. This is to be expected as the gravitational load will be sufficient to complete the failure process once the applied load has reached a critical value to initiate complete failure, which is well before the fracture is complete. The friction angle is only 10^o, and as the angle of the failure slope is greater than this at all points, stable quasi-static growth of the damage is not expected, i.e. friction will not stop gravity collapsing the slope. For the case in Figure 24 the applied load becomes tensile when $\delta = 0.097m$, between the snapshots shown in Figure 24b and 24c, when the failure surface is roughly half formed. Technically after this point the simulation is not strictly valid as some of the interface is subject to a tensile normal stress ($p_n < 0$). This is easily accounted for (by setting the Young's modulus to a very small value) but is not currently in the model. All the models settle at a tensile applied load of $-1.06\ MN/m$. This is greater that the weight of the failed section ($2.1\ MN/m$) which suggests that about half the weight is supported by the frictional interface. The $G_{II} = 1\ kJ/m^2$ curve is truncated as the damage growth rate was too large for the simulation to converge for the lowest fracture energy. Hence Figure 24d is a snapshot of the final state in this case. Overall the proposed viscously regulated model, equation (13), is highly proficient at modelling the very abrupt failure processes that occur in brittle materials. However, in this case the value of $k = 1000s^{-1}$ would need to be reduced to damp down the extremely abrupt failure that occurs for the smallest G_{II} value.

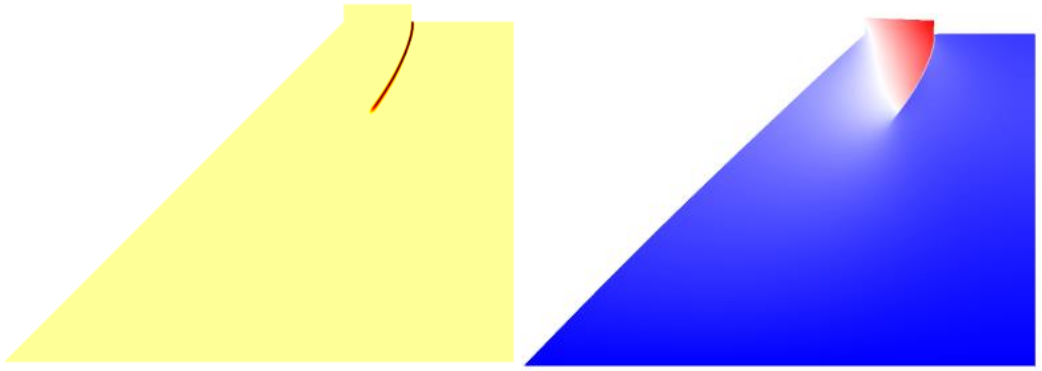

(a)

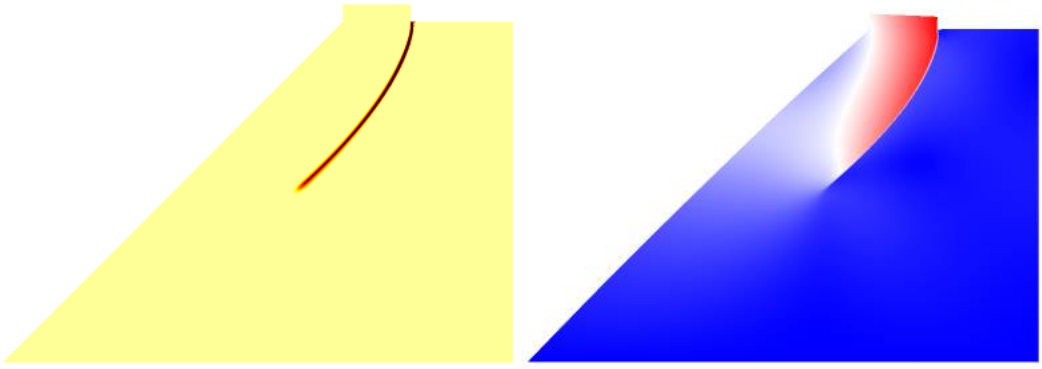

(b)

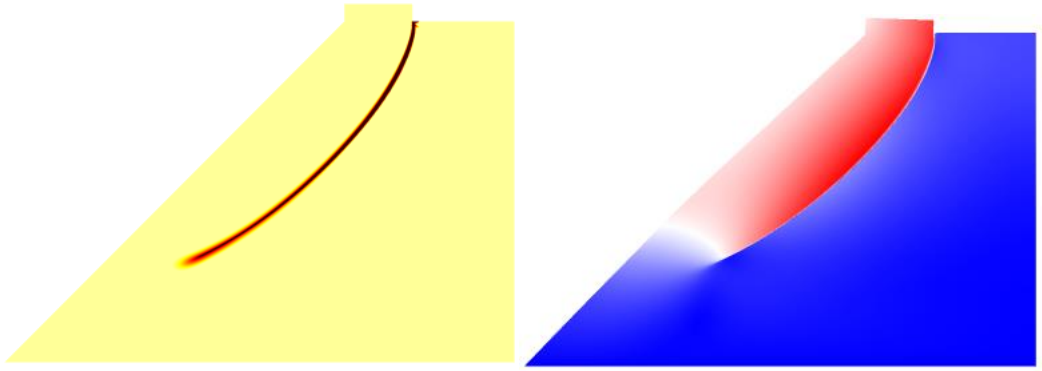

(c)

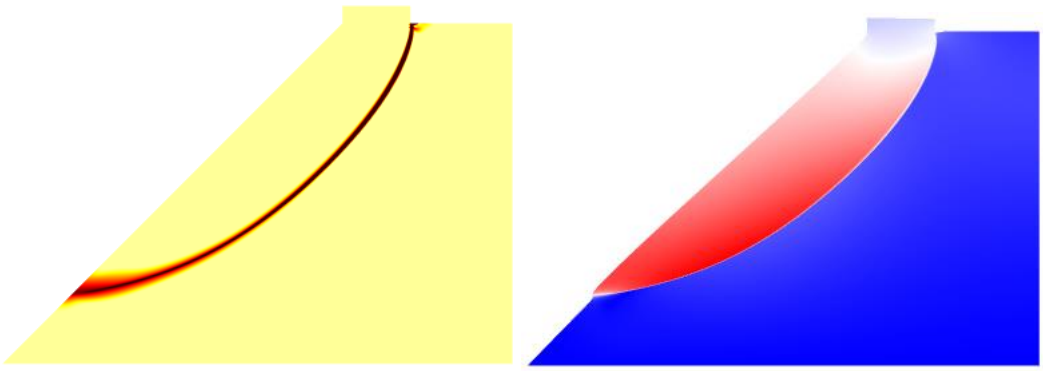

(d)

Figure 24: Slope failure analysis with full gravitational loading using the non-local model with $H = 20m$, $h_{\max} = 0.035m$, $C = 80kPa$ and $G_{II} = 1\ kJ/m^2$ showing damage (left image) and change in the displacement field and deformed shape from the initial condition (right image) at (a) $\delta = 0.093m$, (b) $\delta = 0.096m$, (c) $\delta = 0.099m$ and (d) $\delta = 0.1m$.

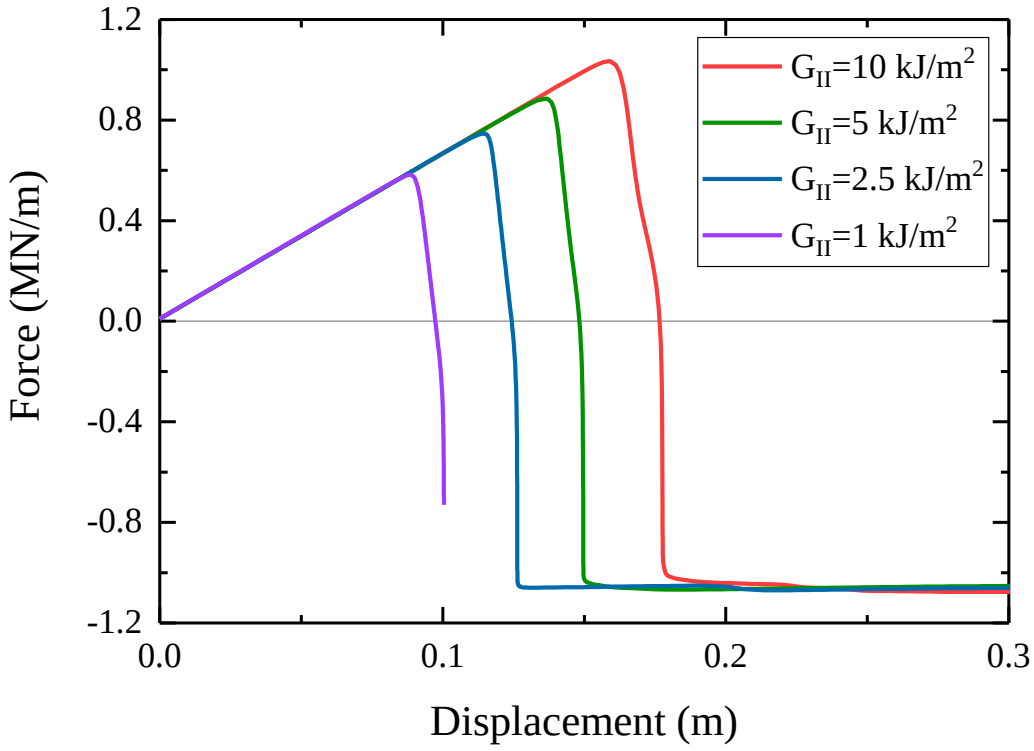

Figure 25: Force-displacement curves for the slope analysis with full gravitational field with $H = 20m$, $h_{\max} = 0.035$ and $C = 80\ kPa$. Results for the non-local model are shown for various values of the shear fracture energy G_{II}, with $G_{II} = 1\ kJ/m^2$ corresponding to Figure 24.

5. Concluding remarks

A damage model for the simulation of compressive, frictional shear crack growth has been proposed and implemented in commercial finite element package COMSOL Multiphysics v5.5. Importantly, the correct crack angle, $\theta = 45^0 - \frac{\phi}{2}$, has been observed in uniaxial and biaxial compression tests. This is due to the anisotropic elasticity modification proposed by Fei and Choo [34,45,46]. The post-failure residual friction force in biaxial compression has been used to validate the friction model. Use of these benchmarks is encouraged to validate other models and offer direct comparison. Supporting the crack face discontinuity using standard elemental shape functions is a compromise: it retains many of the attractive features of the damage models but, as shown in section 3, produces spurious stress perturbations around narrow cracks. It is possible to largely avoid this using very high mesh resolution

for the crack [34] but this is at high computational cost, and reduces the scale of the problem that can be considered. Other methods exist [52] but are not readily implemented in a commercial finite element package. The cost of adopting the proposed method is to introduce the smoothing of two additional measures of the deformation field, the stress normal to the crack face in equation (35) and the rotation field in equation (37). The smoothing lengths are small, so most of the fidelity is retained. The additional computational demand is also small. For triangular elements, the quadratic elastic displacement field has 4 degrees-of-freedom (DOF) per element to represent the horizontal and vertical displacement fields, whereas the linear smoothing fields of the Helmholtz equations introduce just an additional 0.5 DOF per element each.

The model has been developed for the modelling of the growth of dominant cracks in homogeneous brittle materials in two-dimensions where sticking and tensile opening are not considered. Extension of the model to include these additional physical mechanisms, as well as others, such as material heterogeneity [31,32,50], tensile microcracking [31,32], pre-existing shear cracks (e.g. joints [28] or faults [31]), or different frictional shear failure criteria (e.g. Druker-Prager in three-dimensions) are expected to be relatively straightforward within this framework. In large scale geological processes, it is also of interest to explore the interaction between compressive shear failure of faults and hydraulic fracture [16,59-61], interfacial failure [62-64] and the growth of magma intrusions [65,66].

Appendix. Relationship between strain softening response and fracture energy.

Following [67,68], the degraded strain energy in one-dimension is defined as

$$G_{II} = \mathrm{h_{cb}} \int_0^1 \frac{1}{2} \mu \gamma^2 \, dw = \frac{\mu \mathrm{h_{cb}}}{2} \int_{\gamma_0}^{\gamma_f} \gamma^2 \frac{dw}{d\gamma} d\gamma$$

Integrating by parts gives

$$\mathrm{G_{II}} = \frac{\mu \mathrm{h_{cb}}}{2} \left\{ [\gamma^2 w]_{\gamma_0}^{\gamma_f} - 2 \int_{\gamma_0}^{\gamma_f} \gamma w d\gamma \right\}$$

Subtituting $C = \mu\gamma_0$ and equation (4) gives

$$G_{II} = \frac{\mu \mathrm{h_{cb}}}{2} \left\{ \gamma_0^2 + 2\gamma_0 \int_{\gamma_0}^{\gamma_f} g(\gamma) d\gamma \right\} = \mathrm{h_{cb}} C \left[\int_{\gamma_0}^{\gamma_f} g(\gamma) d\gamma + \frac{\gamma_0}{2} \right] \tag{39}$$

which is simply the area under the stress-strain curve in the absence of friction.

Acknowledgements

The funding for this work was provided by an APEX award (Academies Partnership in Supporting Excellence in Cross-disciplinary research award) supported by the Royal Society, the British Academy, the Leverhulme Trust and the Royal Academy of Engineering. The role of the funding source was purely financial support for a research fellowship. The author is grateful to Dr Richard Walker and Dr Catherine Greenfield for useful discussions on structural geology.

References

1. J. C. Jaeger, N. G.W. Cook, R. W. Zimmerman, Fundamentals of Rock Mechanics, Blackwell Publishing, 4th Edition, (2007).
2. T. Saksala, M. Jabareen, Numerical modeling of rock failure under dynamic loading with polygonal elements, International Journal for Numerical and Analytical Methods in Geomechanics, 43 (2019) 2056-2074.
3. J. Dolbow, N. Moés, T. Belytschko, An extended finite element method for modeling crack growth with frictional contact, Computer Methods in Applied Mechanics and Engineering, 190 (51) (2001) 6825–6846.
4. J.-Y. Wu, J.-F. Qiu, V.P. Nguyen, T.K. Mandal, L.-J. Zhuang, Computational modeling of localized failure in solids: XFEM vs PF-CZM, Computer Methods in Applied Mechanics and Engineering, 345 (2019) 618-643.
5. S. Zhou, X. Zhuang, H. Zhu, T. Rabczuk, Phase field modelling of crack propagation, branching and coalescence in rocks, Theoretical and Applied Fracture Mechanics, 96 (2018) 174-192.
6. B. Bourdin, J.J. Marigo, C. Maurini, P. Sicsic, Morphogenesis and propagation of complex cracks induced by thermal shocks, Phys Rev Lett, 112 (2014) 014301.
7. E.C. Bryant, W. Sun, A mixed-mode phase field fracture model in anisotropic rocks with consistent kinematics, Computer Methods in Applied Mechanics and Engineering, 342 (2018) 561-584.
8. R.J.M. Geelen, Y. Liu, T. Hu, M.R. Tupek, J.E. Dolbow, A phase-field formulation for dynamic cohesive fracture, Computer Methods in Applied Mechanics and Engineering, 348 (2019) 680-711.
9. H. Jeong, S. Signetti, T.-S. Han, S. Ryu, Phase field modeling of crack propagation under combined shear and tensile loading with hybrid formulation, Computational Materials Science, 155 (2018) 483-492.
10. X. Lu, C. Li, Y. Tie, Y. Hou, C. Zhang, Crack propagation simulation in brittle elastic materials by a phase field method, Theoretical and Applied Mechanics Letters, 9 (2019) 339-352.
11. R. Ma, W. Sun, FFT-based solver for higher-order and multi-phase-field fracture models applied to strongly anisotropic brittle materials, Computer Methods in Applied Mechanics and Engineering, 362 (2020).
12. C. Miehe, M. Hofacker, L.M. Schänzel, F. Aldakheel, Phase field modeling of fracture in multi-physics problems. Part II. Coupled brittle-to-ductile failure criteria and crack propagation in thermo-elastic–plastic solids, Computer Methods in Applied Mechanics and Engineering, 294 (2015) 486-522.
13. C. Miehe, M. Hofacker, F. Welschinger, A phase field model for rate-independent crack propagation: Robust algorithmic implementation based on operator splits, Computer Methods in Applied Mechanics and Engineering, 199 (2010) 2765-2778.
14. T. Noll, C. Kuhn, D. Olesch, R. Müller, 3D phase field simulations of ductile fracture, GAMM-Mitteilungen, 43 (2019).
15. H.L. Ren, X.Y. Zhuang, C. Anitescu, T. Rabczuk, An explicit phase field method for brittle dynamic fracture, Computers & Structures, 217 (2019) 45-56.
16. M.F. Wheeler, T. Wick, W. Wollner, An augmented-Lagrangian method for the phase-field approach for pressurized fractures, Computer Methods in Applied Mechanics and Engineering, 271 (2014) 69-85.

17. J.-Y. Wu, Robust numerical implementation of non-standard phase-field damage models for failure in solids, Computer Methods in Applied Mechanics and Engineering, 340 (2018) 767-797.
18. X. Zhang, S.W. Sloan, C. Vignes, D. Sheng, A modification of the phase-field model for mixed mode crack propagation in rock-like materials, Computer Methods in Applied Mechanics and Engineering, 322 (2017) 123-136.
19. J.-Y. Wua, Y. Huang, H. Zhou, V. P. Nguyen, Three-dimensional phase-field modeling of mode I + II/III failure in solids, Computer Methods in Applied Mechanics and Engineering, 373 (2020) 113537.
20. A. Staroselsky, R. Acharya, B. Cassenti, Phase field modeling of fracture and crack growth, Engineering Fracture Mechanics, 205 (2019) 268-284.
21. B. Ahmed, G.Z. Voyiadjis, T. Park, A nonlocal damage model for concrete with three length scales, Computational Mechanics, (2021).
22. K. Langenfeld, J. Mosler, A micromorphic approach for gradient-enhanced anisotropic ductile damage, Computer Methods in Applied Mechanics and Engineering, 360 (2020).
23. G. Rastiello, C. Giry, F. Gatuingt, R. Desmorat, From diffuse damage to strain localization from an Eikonal Non-Local (ENL) Continuum Damage model with evolving internal length, Computer Methods in Applied Mechanics and Engineering, 331 (2018) 650-674.
24. S. Sarkar, I.V. Singh, B.K. Mishra, A.S. Shedbale, L.H. Poh, A comparative study and ABAQUS implementation of conventional and localizing gradient enhanced damage models, Finite Elements in Analysis and Design, 160 (2019) 1-31.
25. S. Saroukhani, R. Vafadari, A. Simone, A simplified implementation of a gradient-enhanced damage model with transient length scale effects, Computational Mechanics, 51 (2012) 899-909.
26. H.H. Zhang, L.X. Li, X.M. An, G.W. Ma, Numerical analysis of 2-D crack propagation problems using the numerical manifold method, Engineering Analysis with Boundary Elements, 34 (2010) 41-50.
27. A. Pandolfi, B. Li, M. Ortiz, Modeling fracture by material-point erosion, International Journal of Fracture, 184 (2012) 3-16.
28. Q. Liu, P. Deng, A numerical investigation of element size and loading/unloading rate for intact rock in laboratory-scale and field-scale based on the combined finite-discrete element method, Engineering Fracture Mechanics, 211 (2019) 442-462.
29. G. Li, X.F. Cheng, H. Pu, C.A. Tang, Damage smear method for rock failure process analysis, Journal of Rock Mechanics and Geotechnical Engineering, 11 (2019) 1151-1165.
30. B. Vandoren, A. Simone, Modeling and simulation of quasi-brittle failure with continuous anisotropic stress-based gradient-enhanced damage models, Computer Methods in Applied Mechanics and Engineering, 332 (2018) 644-685.
31. Y. Yuan, T. Xu, M.J. Heap, P.G. Meredith, T. Yang, G. Zhou, A three-dimensional mesoscale model for progressive time-dependent deformation and fracturing of brittle rock with application to slope stability, Computers and Geotechnics, 135 (2021).
32. G.-l. Zhou, T. Xu, M.J. Heap, P.G. Meredith, T.M. Mitchell, A.S.-Y. Sesnic, Y. Yuan, A three-dimensional numerical meso-approach to modeling time-independent deformation and fracturing of brittle rocks, Computers and Geotechnics, 117 (2020).
33. B. Bahmani, R. Abedi, P. Clarke, A Stochastic Bulk Damage Model Based on Mohr-Coulomb Failure Criterion for Dynamic Rock Fracture, Applied Sciences, 9 (2019).
34. F. Fei, J. Choo, A phase-field model of frictional shear fracture in geologic materials, Computer Methods in Applied Mechanics and Engineering, 369 (2020).

35. T. You, Q.-Z. Zhu, P.-F. Li, J.-F. Shao, Incorporation of tension-compression asymmetry into plastic damage phase-field modeling of quasi brittle geomaterials, International Journal of Plasticity, 124 (2020) 71-95.
36. S. Zhou, X. Zhuang, T. Rabczuk, Phase field modeling of brittle compressive-shear fractures in rock-like materials: A new driving force and a hybrid formulation, Computer Methods in Applied Mechanics and Engineering, 355 (2019) 729-752.
37. J. Choo, W. Sun, Coupled phase-field and plasticity modeling of geological materials: From brittle fracture to ductile flow, Computer Methods in Applied Mechanics and Engineering, 330 (2018) 1-32.
38. A. Spetz, R. Denzer, E. Tudisco, O. Dahlblom, Phase-field fracture modelling of crack nucleation and propagation in porous rock, International Journal of Fracture, 224 (2020) 31-46.
39. Z. Song, H. Konietzky, M. Herbst, Bonded-particle model-based simulation of artificial rock subjected to cyclic loading, Acta Geotech, 14 (2019) 955–971.
40. J. Bi, X.P. Zhou, Q.H. Qian, The 3D Numerical Simulation for the Propagation Process of Multiple Pre-existing Flaws in Rock-Like Materials Subjected to Biaxial Compressive Loads, Rock Mechanics and Rock Engineering, 49 (2015) 1611-1627.
41. H. Hofmann, T. Babadagli, G. Zimmermann, A grain based modeling study of fracture branching during compression tests in granites, International Journal of Rock Mechanics and Mining Sciences, 77 (2015) 152-162.
42. H.H. Ruan, L.C. Zhang, J. Lu, A new constitutive model for shear banding instability in metallic glass, International Journal of Solids and Structures, 48 (2011) 3112-3127.
43. R. Alessi, F. Freddi, L. Mingazzi, Phase-field numerical strategies for deviatoric driven fractures, Computer Methods in Applied Mechanics and Engineering, 359 (2020).
44. M.E. Mobasher, L. Berger-Vergiat, H. Waisman, Non-local formulation for transport and damage in porous media, Computer Methods in Applied Mechanics and Engineering, 324 (2017) 654-688.
45. F. Fei, J. Choo, A phase-field method for modeling cracks with frictional contact, International Journal for Numerical Methods in Engineering, 121 (2019) 740-762.
46. F. Fei, J. Choo, Double-phase-field formulation for mixed-mode fracture in rocks, Computer Methods in Applied Mechanics and Engineering, 376 (2021).
47. T.K. Mandal, V.P. Nguyen, A. Heidarpour, Phase field and gradient enhanced damage models for quasi-brittle failure: A numerical comparative study, Engineering Fracture Mechanics, 207 (2019) 48-67.
48. D.T. Le, J.-J. Marigo, C. Maurini, S. Vidoli, Strain-gradient vs damage-gradient regularizations of softening damage models, Computer Methods in Applied Mechanics and Engineering, 340 (2018) 424-450.
49. Y. Lu, D. Elsworth, L. Wang, A dual-scale approach to model time-dependent deformation, creep and fracturing of brittle rocks, Computers and Geotechnics, 60 (2014) 61-76.
50. T. You, H. Waisman, Q.-Z. Zhu, Brittle-ductile failure transition in geomaterials modeled by a modified phase-field method with a varying damage-driving energy coefficient, International Journal of Plasticity, 136 (2021).
51. A.C. Palmer, J.R. Rice, The growth of slip surfaces in the progressive failure of over-consolidated clay, Proc. R. Soc. Lond. Ser. A Math. Phys. Eng. Sci. 332 (1591) (1973) 527–548.
52. R. Borja, Plasticity. Modeling and computation, Springer (2013). https://doi.org/10.1007/978-3-642-38547-6

53. E.C. Bryant, W. Sun, Phase field modeling of frictional slip with slip weakening/strengthening under non-isothermal conditions, Computer Methods in Applied Mechanics and Engineering, 375 (2021).
54. D.E. Moore and D.A.Lockner, The role of microcracking in the shear fracture propagation of granite, Journal of Structural Geology, 17 (1) (1995) 95-114.
55. J. Choo, A. Sohail, F. Fei, T.-f. Wong, Shear fracture energies of stiff clays and shales, Acta Geotechnica, (2021).
56. L.H. Poh, G. Sun, Localizing gradient damage model with decreasing interactions, International Journal for Numerical Methods in Engineering, 110 (2017) 503-522.
57. R. A. Regueiro, R. I. Borja, Plane strain finite element analysis of pressure sensitive plasticity with strong discontinuity, International Journal of Solids and Structures,38 (21) (2001) 3647-3672. https://doi.org/10.1016/S0020-7683(00)00250-X
58. X. Xiang, D. Zi-Hang, Numerical implementation of a modified Mohr–Coulomb model and its application in slope stability analysis, Journal of Modern Transportation, 25 (2017) 40-51.
59. B. Giovanardi, S. Serebrinsky, R. Radovitzky, A fully-coupled computational framework for large-scale simulation of fluid-driven fracture propagation on parallel computers, Computer Methods in Applied Mechanics and Engineering, 372 (2020).
60. Y. Heider, W. Sun, A phase field framework for capillary-induced fracture in unsaturated porous media: Drying-induced vs. hydraulic cracking, Computer Methods in Applied Mechanics and Engineering, 359 (2020).
61. M. Vahab, S. Akhondzadeh, A.R. Khoei, N. Khalili, An X-FEM investigation of hydro-fracture evolution in naturally-layered domains, Engineering Fracture Mechanics, 191 (2018) 187-204.
62. A.C. Hansen-Dörr, R. de Borst, P. Hennig, M. Kästner, Phase-field modelling of interface failure in brittle materials, Computer Methods in Applied Mechanics and Engineering, 346 (2019) 25-42.
63. H. Henry, Limitations of the modelling of crack propagating through heterogeneous material using a phase field approach, Theoretical and Applied Fracture Mechanics, 104 (2019).
64. J. Reinoso, P. Durand, P. Budarapu, M. Paggi, Crack Patterns in Heterogenous Rocks Using a Combined Phase Field-Cohesive Interface Modeling Approach: A Numerical Study, Energies, 12 (2019).
65. R.J. Walker, S.P.A. Gill, Tectonic stress controls saucer-shaped sill geometry and emplacement mechanism, Geology 48 (9) (2020) 898–902 https://doi.org/10.1130/G47604.1.
66. S.P.A. Gill, R.J. Walker, The Roles of Elastic Properties, Magmatic Pressure, and Tectonic Stress in Saucer-Shaped Sill Growth, Journal of Geophysical Research: Solid Earth, 124 (2020) https://doi.org/10.1029/2019JB019041
67. Z.P. Bažant, B.H. Oh, Crack band theory for fracture of concrete, Matériaux et Constructions, 16 (1983) 155-177.
68. J. Oliver, M. Cervera, S. Oller, J. Lubliner, Isotropic Damage Models and Smeared Crack Analysis of Concrete, Computer Aided Analysis and design of Concrete Structures, Proceedings of SCI-C 1990, II. International Conference. (Austria, 1990) 945–957.